

## III-nitride semiconductors for intersubband optoelectronics: a review

This content has been downloaded from IOPscience. Please scroll down to see the full text.

2013 Semicond. Sci. Technol. 28 074022

(<http://iopscience.iop.org/0268-1242/28/7/074022>)

View [the table of contents for this issue](#), or go to the [journal homepage](#) for more

Download details:

IP Address: 103.21.125.82

This content was downloaded on 11/01/2017 at 17:19

Please note that [terms and conditions apply](#).

You may also be interested in:

[GaN/AlGaIn intersubband optoelectronic devices](#)

H Machhadani, P Kandaswamy, S Sakr et al.

[Polar and nonpolar GaN quantum dots](#)

Bruno Daudin

[Photodetectors based on intersubband transitions using III-nitride superlattice structures](#)

Daniel Hofstetter, Esther Baumann, Fabrizio R Giorgetta et al.

[Quantum dot optoelectronic devices: lasers, photodetectors and solar cells](#)

Jiang Wu, Siming Chen, Alwyn Seeds et al.

[Recent progress in quantum cascade lasers and applications](#)

Claire Gmachl, Federico Capasso, Deborah L Sivco et al.

[Growth and applications of Group III-nitrides](#)

O Ambacher

[N-polar GaN epitaxy and high electron mobility transistors](#)

Man Hoi Wong, Stacia Keller, Nidhi, Sansaptak Dasgupta et al.

[Nonpolar m-plane GaN/AlGaIn heterostructures with intersubband transitions in the 5–10 THz band](#)

C B Lim, A Ajay, C Bougerol et al.

## INVITED REVIEW

# III-nitride semiconductors for intersubband optoelectronics: a review

M Beeler, E Trichas and E Monroy

CEA-Grenoble, INAC/SP2M/NPSC, 17 rue des Martyrs, 38054 Grenoble, France

E-mail: [eva.monroy@cea.fr](mailto:eva.monroy@cea.fr)

Received 3 December 2012, in final form 19 January 2013

Published 21 June 2013

Online at [stacks.iop.org/SST/28/074022](http://stacks.iop.org/SST/28/074022)

## Abstract

III-nitride nanostructures have recently emerged as promising materials for new intersubband (ISB) devices in a wide variety of applications. These ISB technologies rely on infrared optical transitions between quantum-confined electronic states in the conduction band of GaN/Al(Ga)N nanostructures, namely quantum wells or quantum dots. The large conduction band offset (about 1.8 eV for GaN/AlN) and sub-picosecond ISB relaxation of III-nitrides render them appealing materials for ultrafast photonic devices in near-infrared telecommunication networks. Furthermore, the large energy of GaN longitudinal-optical phonons (92 meV) opens prospects for high-temperature THz quantum cascade lasers and ISB devices covering the 5–10 THz band, inaccessible to As-based technologies due to phonon absorption. In this paper, we describe the basic features of ISB transitions in III-nitride quantum wells and quantum dots, in terms of theoretical calculations, material growth, spectroscopy, resonant transport phenomena, and device implementation. The latest results in the fabrication of control-by-design devices such as all-optical switches, electro-optical modulators, photodetectors, and lasers are also presented.

(Some figures may appear in colour only in the online journal)

## 1. Introduction

### 1.1. Historical introduction

Semiconductor materials can be made optically active at infrared (IR) wavelengths regardless of their band gap by engineering the electron quantum confinement in thin layers. Such controlled-by-design devices rely on optical intersubband (ISB) transitions between electronic confined states, and the desired transitional wavelength can be obtained through engineering of the layer thicknesses. The first studies of ISB absorption date back to 1974, when Kamgar *et al* [1] recorded optical transitions between bound electronic levels in an accumulation layer on *n*-type Si(100) under far-IR illumination. Since then, a number of works on Si space-charge regions and III–V surface layers have contributed to a more detailed understanding of quantum confinement in thin-film structures, many-body effects, ISB absorption selection rules, oscillator strengths and line shapes [2]. The

extrapolation of these principles to GaAs/AlGaAs quantum wells (QWs) to shift the transition wavelength to the mid-IR was first suggested by Esaki and Sakaki [3], and subsequent experimental [4, 5] and theoretical studies [6, 7] led to the first experimental measurement of strong ISB absorption in a series of multiple QWs (MQWs), performed by West and Eglash [8]. These results set the basis for the fabrication of the first QW infrared photodetector (QWIP), by Levine *et al* [9, 10]. In 1994, Faist *et al* [11] presented a major breakthrough in the ISB technology: an alternative to the conventional laser diode, with a novel operating principle—the quantum cascade laser (QCL). This was the beginning of tremendous development of the ISB technology which resulted in commercially available devices operating in the mid- and far-IR.

Nowadays, ISB optoelectronic devices (photodetectors and emitters) based on the III-As material system (GaAs/AlGaAs, InGaAs/AlInAs, or GaInAs/AlAsSb) can be tuned from the mid-IR to the THz spectral range. Operation at shorter wavelengths (<3  $\mu\text{m}$ ) is limited by the

available conduction band offset and by material transparency. III-nitride semiconductors (GaN, AlN, InN and their alloys), with their wide band gap and a large conduction band offset ( $\sim 1.8$  eV for GaN/AlN [12–14]), are attracting much interest for ISB devices operating in the near-IR spectral range, particularly in the 1.3–1.55  $\mu\text{m}$  wavelength window used for fiber-optic communications [15–17]. GaN is transparent in a large spectral region, notably for wavelengths longer than 360 nm (band gap), except for the Reststrahlen band (from 9.6 to 19  $\mu\text{m}$ ). Absorption in the range of 7.3 to 9  $\mu\text{m}$  has been observed in bulk GaN substrates with carrier concentrations  $< 10^{16} \text{ cm}^{-3}$  [18–20], and was attributed to the second harmonic of the Reststrahlen band. Although this second band might hinder the fabrication of waveguided devices in this spectral region, its effect in planar devices with  $\mu\text{m}$ -sized active regions (for instance, QWIPs) is negligible. This is because the absorption coefficient related to two-phonon processes is much smaller than the one associated with ISB transitions. This has been experimentally demonstrated by the identification of ISB absorption in AlGaIn/GaN QWs within such a band [21, 22]. On the other hand, III-nitrides do not present problems of inter-valley scattering, since the L and X points are much higher in energy ( $> 2$  eV) than the  $\Gamma$  point.

The feasibility of a GaN-based ISB technology in the telecommunication spectral range was early predicted by Suzuki *et al* [15, 23], who additionally estimated an ISB relaxation time around 80 fs at 1.55  $\mu\text{m}$ , i.e. about 30 times shorter than that in InGaAs QWs, and high third-order nonlinear susceptibility (around  $1.6 \times 10^{-15} \text{ m}^2 \text{ V}^{-2}$  for a carrier concentration  $n = 1 \times 10^{18} \text{ cm}^{-3}$ ). These characteristics led them to propose GaN/AlGaIn QWs as the active media for multi-terabit/s ISB all-optical switches. In the next decade, their prediction proved valid and the first prototypes of GaN-based ISB devices operating at 1.55  $\mu\text{m}$  have closely fulfilled their expectations.

On the other hand, there is an interest to push the III-nitride ISB technology toward longer wavelengths, particularly to the THz frequency range. The potential of this spectral region in applications like security screening, quality control and medical diagnostics has driven extensive development of optoelectronic components. Due to the large LO-phonon energy of GaN (about three times that of GaAs), room temperature operation becomes feasible for ISB devices covering the IR band that was typically inaccessible to As-based semiconductors due to phonon absorption.

### 1.2. Physics of intersubband transitions: polarization selection rule

For a comprehensive introduction to ISB physics in QWs, we refer the readers to the work of Bastard [24] or Liu and Capasso [25]. In this section, we briefly introduce the polarization selection rule characteristic of ISB transitions in QWs and we derive an expression for the ISB absorption coefficient. For this purpose, we consider a QW with two confined states in a single-particle approach. Any transition from a state  $i$  to a state  $f$ , interband or ISB, can be described with Fermi's golden rule:

$$W_{fi} = \frac{2\pi}{\hbar} |\langle \psi_f | H' | \psi_i \rangle|^2 \delta(E_f - E_i - \hbar\omega), \quad (1)$$

where  $H'$  is the interaction Hamiltonian,  $\hbar\omega$  is the radiation energy, and  $\psi$  and  $E$  are the wave functions and energies of the confinement levels for the initial ( $i$ ) and final ( $f$ ) states. As the radiation wavelength is much larger than the lattice periodicity in the case of interband transitions, and larger than the QW width in the case of ISB transitions, it is possible to apply the dipole approximation:

$$H' = \frac{q^2 F_0^2}{4m^* \omega^2} (\vec{\varepsilon} \cdot \vec{p}), \quad (2)$$

where  $q$  denotes elementary charge,  $F_0$  is the electric field amplitude,  $m^*$  is effective mass, and  $\vec{\varepsilon}$  and  $\vec{p}$  are the polarization vector and the momentum operator, respectively. Substituting equation (2) in equation (1) we obtain

$$W_{fi} = \frac{2\pi}{\hbar} \frac{q^2 F_0^2}{4m^* \omega^2} |\langle \psi_f | \vec{\varepsilon} \cdot \vec{p} | \psi_i \rangle|^2 \delta(E_f - E_i - \hbar\omega). \quad (3)$$

Applying the envelop function formalism, the wavefunction of an electron  $\psi_i(\vec{r})$  can be expressed as a product of a periodic Bloch function,  $u_v(\vec{r})$ , and a slowly varying envelope function,  $f_n(\vec{r})$ , where  $n$  denotes the quantum numbers of the problem. Under the assumption that the lattice-periodic function is the same in all constituent materials a Schrödinger equation only for the envelope function can be derived:

$$-\frac{\hbar^2}{2m^*} \nabla^2 f_n(\vec{r}) + V(\vec{r}) f_n(\vec{r}) = E_n f_n(\vec{r}), \quad (4)$$

where  $V(\vec{r})$  is the potential profile and  $E_n$  are the energy eigenvalues. Introducing the envelop function expression in a QW:

$$f_n(\vec{r}) = \frac{1}{\sqrt{S}} \exp(i\vec{k}_\perp \cdot \vec{r}_\perp) \chi(z), \quad (5)$$

where  $S$  is the sample area,  $\chi(z)$  is the envelop function component along the growth axis, and  $\vec{k}_\perp$  and  $\vec{r}_\perp$  denote the two-dimensional (2D) vectors ( $k_x, k_y$ ) and ( $x, y$ ), the solution of equation (4) leads to energy eigenvalues of the form

$$E_n(k_\perp) = E_{n0} + \frac{\hbar^2 k_\perp^2}{2m^*}, \quad (6)$$

where the subband energies  $E_{n0}$  depend on the potential profile  $V(z)$ . For a symmetric QW with infinite barriers, the following eigenvalues are obtained:

$$E_n(k_\perp) = \frac{n^2 \hbar^2 k_\perp^2}{2m^* L^2} + \frac{\hbar^2 k_\perp^2}{2m^*}, \quad (7)$$

where  $L$  is the QW thickness. Note that, due to the relatively large electron effective mass of GaN ( $m^*/m_0 \sim 0.2$ ) compared to GaAs ( $m^*/m_0 \sim 0.067$ ) or InAs ( $m^*/m_0 \sim 0.023$ ), very thin GaN QWs are required to attain large ISB transition energies.

Coming back to equation (3), the matrix element  $\langle \psi_f | \vec{\varepsilon} \cdot \vec{p} | \psi_i \rangle$  splits into

$$\langle \psi_f | \vec{\varepsilon} \cdot \vec{p} | \psi_i \rangle = \vec{\varepsilon} \cdot \langle u_v | \vec{p} | u_{v'} \rangle \langle f_n | f_{n'} \rangle + \vec{\varepsilon} \cdot \langle u_v | u_{v'} \rangle \langle f_n | \vec{p} | f_{n'} \rangle, \quad (8)$$

where  $v$  and  $v'$  and  $n$  and  $n'$  are the band and subband indices of final and initial states, respectively. The first term describes the interband transitions and it vanishes in the case of transitions within the same band. It consists of a dipole matrix element of Bloch functions, which dictates the

interband polarization selection rules, and an overlap integral of the envelope functions, which gives rise to selection rules concerning the electron and hole subband quantum numbers. The second term represents the ISB processes, and it consists of an overlap integral of Bloch functions, which is nonzero when two envelope states are taken from the same band, and a dipole matrix element of the envelope functions, which defines the *polarization selection rule*:

$$\langle f_n | \vec{\epsilon} \cdot \vec{p} | f_n' \rangle = \frac{1}{S} \epsilon_z \delta(k_{\perp}^i - k_{\perp}^f) \int dz \chi_n^*(z) p_z \chi_n'(z). \quad (9)$$

Thus, only the  $z$ -component of the electric field couples to the ISB transition, i.e. structures respond only to transverse-magnetic (TM) polarized light, which imposes the use of surface gratings or waveguide configurations to couple the light into the active region.

Inserting equation (9) in equation (3) and taking into account that the momentum can be described as  $\vec{p}_{nm'} = im * \omega \vec{r}_{nm'}$ , the ISB transition rate can be rewritten as

$$W_{fi} = \frac{2\pi}{\hbar} \frac{q^2 F_0^2}{4} \epsilon_z^2 |\langle \chi_f(z) | z | \chi_i(z) \rangle|^2 \times \delta(k_{\perp}^i - k_{\perp}^f) \delta(E_f - E_i - \hbar\omega). \quad (10)$$

The ISB absorption coefficient between states  $i$  and  $f$  is usually defined through the ratio of the absorbed electromagnetic energy per unit time and volume,  $\hbar\omega W_{fi}/V$ , and the intensity of the incident radiation,  $I = \frac{1}{2} n c \epsilon_0 F_0^2$ ; where  $\epsilon_0$  is the vacuum permittivity,  $n$  is the refractive index of the material and  $c$  is the speed of light:

$$\alpha(\omega) = \frac{\pi q^2 (E_f - E_i)}{n c \epsilon_0 \hbar V} \times \epsilon_z^2 \sum_{i,f} 2 |\langle \chi_f(z) | z | \chi_i(z) \rangle|^2 [f(E_i) - f(E_f)] \delta(E_f - E_i - \hbar\omega), \quad (11)$$

with  $f(E)$  being the Fermi function. The sum can be expressed as the difference of carrier surface density of the two subbands,  $n_i^S - n_f^S$ :

$$\sum_{i,f} 2 [f(E_i) - f(E_f)] = S (n_i^S - n_f^S), \quad (12)$$

where  $S$  is the crystal surface. Therefore, the ISB absorption coefficient between two subbands can be written as

$$\alpha(\omega) = \frac{\pi (E_f - E_i)}{n c \epsilon_0 \hbar L} (n_i^S - n_f^S) \epsilon_z^2 \mu_{if}^2 \delta(E_f - E_i - \hbar\omega), \quad (13)$$

where  $\mu_{if} = q \langle \chi_f(z) | z | \chi_i(z) \rangle$  is the ISB dipole matrix element.

The dipole matrix element only involves the envelope wavefunctions for the initial and final subbands. Thus, as  $z$  is odd, *only transitions between subbands with opposite parity of the envelope wavefunctions are allowed in symmetric QWs*. This selection rule does not apply for asymmetric potential profiles.

The coupling efficiency between the two subbands is given by the oscillator strength, which is shown as

$$F_{if} = \frac{2m_0 (E_f - E_i)}{q^2 \hbar^2} \mu_{if}^2. \quad (14)$$

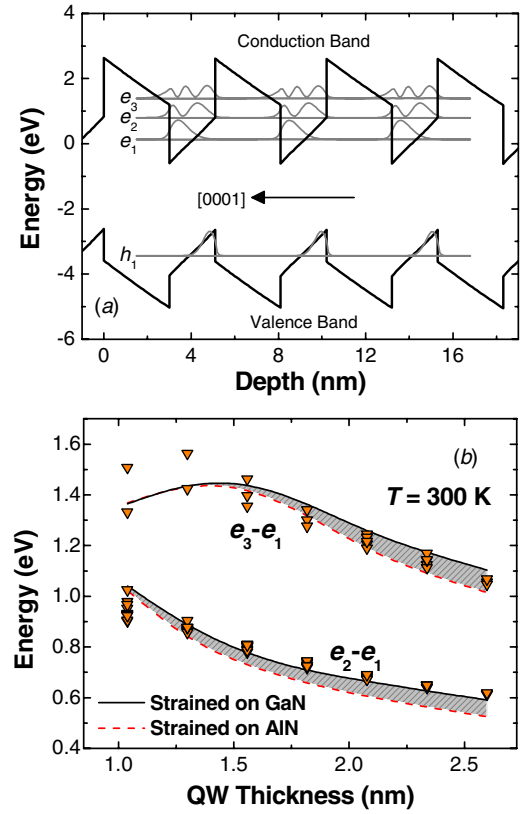


**Figure 1.** (a) Band diagram of GaN/AlN QWs in an infinite superlattice with 3 nm thick AlN barriers and 2 nm thick GaN QWs. The structure is considered strained on an AlN substrate. The electron wavefunctions of the ground hole state,  $h_1$ , the ground electron state,  $e_1$ , and the excited electron states,  $e_2$  and  $e_3$ , are presented. (b) Variation of the  $e_2-e_1$  and  $e_3-e_1$  ISB transition energy as a function of the QW thickness in GaN/AlN MQW structures with 3 nm thick barriers. Triangles indicate experimental data and solid and dashed lines correspond to theoretical calculations assuming the structure fully strained on AlN and on GaN substrates, respectively. Reprinted with permission from [28]. Copyright 2008, American Institute of Physics.

## 2. Intersubband absorption in III-nitride nanostructures

### 2.1. GaN/AlGaIn polar quantum wells

**2.1.1. Modeling.** The optical properties of (0001)-oriented nitride QWs are strongly affected by the presence of an internal electric field arising from the piezoelectric and spontaneous polarization discontinuity between the well and barrier materials [26]. This is one of the most influential characteristics of III-nitride semiconductors, and plays a major role in determining the band structure. Figure 1(a) presents the band diagram of a GaN/AlN (2 nm/3 nm) superlattice calculated using the nextnano3 8-band k.p Schrödinger–Poisson solver [27] with the material parameters described in [28]. The structures were considered strained on the AlN substrate. The electronic potential takes on a characteristic saw-tooth profile due to the internal electric field. The electron wavefunctions of the ground hole state  $h_1$ , the ground electron state  $e_1$  and the excited electron states  $e_2$  and  $e_3$  are presented in the figure. Due to the built-in electric field, the electron



wavefunctions are shifted toward the  $[0001]$  direction and the hole wavefunctions toward the  $[00\bar{0}1]$  direction (quantum-confined Stark effect, QCSE). In narrow QWs ( $\sim 1$  nm) the energy difference between  $e_1$  and  $e_2$  is mostly determined by the confinement in the QW, whereas for larger QWs ( $> 2$  nm) this difference is mostly determined by the QCSE, since both electronic levels lie in the triangular part of the QW potential profile. A detailed description of the evolution of the ISB transitions  $e_2-e_1$  and  $e_3-e_1$  with the QW thickness and strain state is presented in figure 1(b) and compared with experimental data from GaN/AlN MQWs. The increase in the  $e_2-e_1$  ISB energy difference in the calculations for the MQW strained on GaN is related to the enhanced electric field, due to the larger piezoelectric coefficients of the AlN barrier in comparison to the GaN QW [28].

The band structure simulations show that certain QW thicknesses can result in a configuration where the  $e_1 \rightarrow e_2$  transition has approximately the same energy as the  $e_2 \rightarrow e_3$  (or for very thick barrier layers the  $e_2 \rightarrow e_4$ ) transition. This is an interesting experimental situation because it can result in the enhancement of second-order and third-order nonlinear effects such as two-photon absorption [29], second-harmonic generation [30] or saturable absorption [31].

In nitride heterostructures, the charge distribution depends not only on the Si doping level in the QWs, but also on the presence of non-intentional dopants and on the carrier redistribution due to the internal electric field. The polarization discontinuity between heterostructure layers leads to strong band bendings, which typically result in the formation of a depletion layer on one side of the active region and an accumulation layer on the other side (see figure 2(a)). Therefore, a realistic view of the charge distribution in a device is only achieved by extending the electronic modeling to the complete structure. As an illustration of this phenomena, Kandaswamy *et al* have studied the contribution of the internal electric field induced by a 50 nm thick  $\text{Al}_x\text{Ga}_{1-x}\text{N}$  cap layer to the ISB absorption of 40-period non-intentionally doped GaN/AlN (1.5/1.5 nm) MQWs grown on AlN [28]. The Al mole fraction of the cap layer was  $x = 0, 0.25, 0.5$  and 1 for the samples under study. Measurements of ISB absorption in these samples, presented in figure 2(c), confirm a monotonic increase and broadening of the absorption when increasing the Al mole fraction of the cap layer. These results are consistent with the simulations of the electronic structure in figures 2(a) and (b), where we observe that the use of AlN as a cap layer lowers the conduction band of the first GaN QWs below the Fermi level (dash-dotted line at 0 eV in the figures), whereas the use of GaN as a cap layer results in the depletion of the MQW active region. Therefore, we conclude that the internal electric field induced by the cap layer can result in a significant (even dominant) contribution to the infrared absorption in GaN/AlN MQW structures.

**2.1.2. Growth and defect analysis.** A main requirement for the growth of the III-nitride nanostructures required for ISB devices is a precise control of the thickness and interfaces. Molecular-beam epitaxy (MBE) seems to be the most suitable technique for this application thanks to its

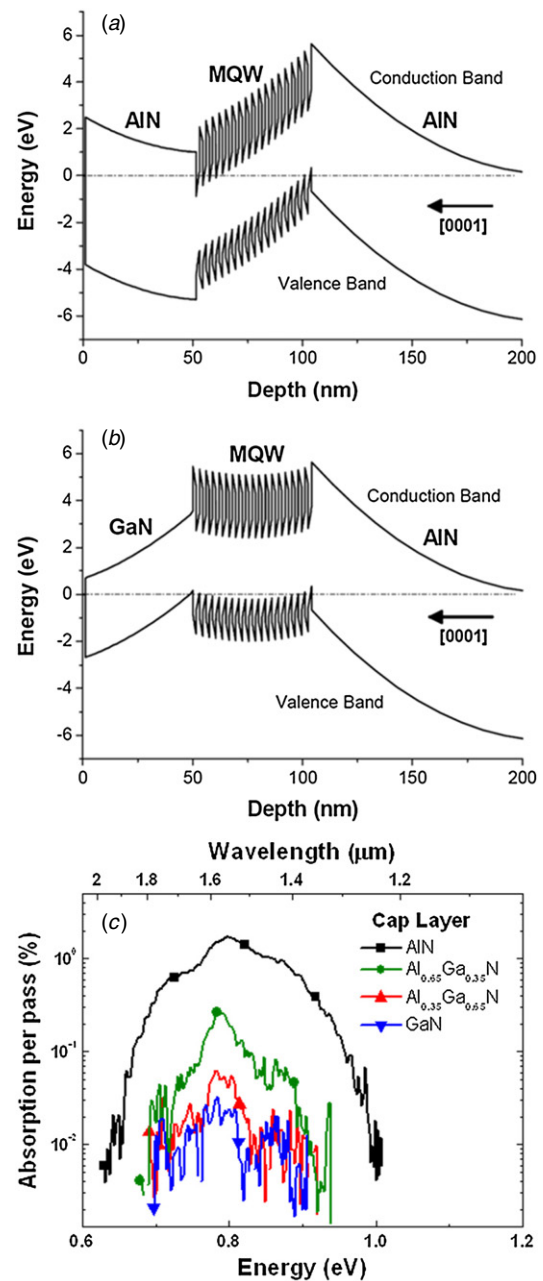


**Figure 2.** Band diagram of nonintentionally doped GaN/AlN (1.5/1.5 nm) MQW structures with (a) AlN cap layer and (b) GaN cap layer. (c) Room-temperature TM-polarized ISB absorption spectra of nonintentionally doped GaN/AlN (1.5/1.5 nm) MQW structures finished with a 50 nm thick  $\text{Al}_x\text{Ga}_{1-x}\text{N}$  cap layer with different Al mole fractions. Reprinted with permission from [28]. Copyright 2008, American Institute of Physics.

low growth temperature that hinders GaN-AlN interdiffusion [32]. Plasma-assisted MBE (PAMBE) was the first method to produce III-nitride nanostructures displaying ISB transitions at telecommunication wavelengths (1.3, 1.55  $\mu\text{m}$ ) [33–39]. The growth of (0001)-oriented GaN, AlN and AlGa<sub>N</sub> by PAMBE is extensively discussed in the literature [40–45]. Deposition of III-nitride 2D layers requires a precise control of the III/V flux ratio during the growth; particularly, it demands slightly metal-rich conditions, and hence growth optimization requires the determination of stoichiometric flux conditions

and precise control of the growth temperature. In the case of GaN, at a substrate temperature higher than 700 °C, there is a certain range of Ga fluxes for which the Ga excess remains in a situation of dynamic equilibrium on the growing front, i.e. the Ga coverage is independent of the Ga exposure time. Smooth surfaces are generally achieved under a moderate Ga excess [40, 42, 46, 47], when the Ga excess arranges into a so-called laterally-contracted Ga bilayer, which consists of two Ga layers adsorbed on the Ga-terminated (0001) GaN surface [40, 41, 47–49]. Some groups prefer growing under higher Ga fluxes, in the droplet formation regime. They periodically consume the Ga excess by shuttering the Ga cell and exposing the surface to active nitrogen [50, 51]. This method provides high-quality layers, but it is important to predict the additional GaN thickness from consuming the excess, which depends on the impinging Ga flux, the active nitrogen flux and the substrate temperature. Finally, it has also been reported that smooth surface morphologies can be achieved via stoichiometric growth at high temperature (~780–790 °C), when GaN decomposition is already active [52]. However, this growth method has not been applied to ISB devices or GaN/AlGaIn QWs, and problems associated with material interdiffusion are expected [53].

An alternative to the above-described GaN growth conditions is the use of a surfactant to promote 2D growth [54]. Indium has been reported to behave as a surfactant for the PAMBE growth of (Al,Ga)N, since it favors 2D growth under slightly N-rich conditions [41, 44, 55–57]. The utility of this growth method to synthesize GaN/AlN QWs displaying ISB absorption has been demonstrated [28].

In the case of AlN, the deposition of layers with atomically flat surface morphology also requires metal-rich conditions [45]. However, Al does not desorb from the surface at the standard growth temperature for GaN. Therefore, to eliminate the Al excess at the surface, it is necessary to perform periodic growth interruptions under nitrogen. An alternative approach to achieve 2D growth of AlN and low Al content (<50%) Al(Ga)N layers is to use Ga (or In) as a surfactant, with the Al flux corresponding to the required Al mole fraction [28, 43, 58].

GaN/AlN QWs displaying ISB transitions in the near-IR can also be synthesized by metalorganic vapor phase epitaxy (MOVPE) [59–61]. In this case, a critical parameter to attain devices in the telecommunication spectral range (1.3 μm, 1.55 μm) is the reduction of the growth temperature from the 1050–1100 °C optimum range for GaN growth down to 900–950 °C (or even to 770 °C [62]), in order to minimize the GaN-AlN interdiffusion. Furthermore, deposition under compressive strain (e.g. using AlN substrates) is recommended at these growth temperatures to prevent the red shift of the ISB transition due to instabilities of the GaN/AlN interface [63].

Since GaN/AlN is a lattice mismatched system (2.5% in-plane lattice mismatch), it is important to understand the effects of strain and misfit relaxation at the contact layer/active region interface, as well as the strain generated by layer alternation within the active region of the ISB device. The mechanisms of strain relaxation can be elastic, i.e. undulation of the surface, or plastic, i.e. by introduction of extended

defects, which can affect the device properties causing nonradiative recombination, carrier scattering, or enhanced diffusion of dopants and impurities. There are several types of plastic relaxation: crack propagation (commonly observed in III-nitrides under tensile stress), decohesion of the layer, introduction of misfit dislocations (MDs) or glide of pre-existing threading dislocations (TDs). The density of edge-type TDs should be kept to a minimum since they cause losses in the transmission of TM polarized light, which adversely affects the performance of ISB devices [64]. These TDs propagate from the heteroepitaxial substrates (typical TD densities in commercial GaN-on-sapphire or AlN-on-sapphire templates are in the 10<sup>8</sup> cm<sup>-2</sup> and 10<sup>9</sup> cm<sup>-2</sup> range, respectively), but they are also generated during the growth due to the plastic strain relaxation, since MDs often fold toward the growth direction, giving rise to the edge-type TDs [65].

Plastic relaxation in semiconductors with cubic symmetry, such as silicon and GaAs, usually takes place along the {110} {111} main slip system, either by nucleation of dislocation half loops at the growth surface or by bowing of pre-existing threading dislocations into the heterointerface [66]. However, it is not clear how semiconductors with hexagonal symmetry, such as III nitrides, relax the misfit stress. In the case of nitride heterostructures grown along the [0001] axis, the formation of regular networks of MDs is hindered since the most crystallographically favorable slip system, the (0001) basal plane with {11-20} {0002} slip directions, lies parallel to the heterointerfaces. This means that the resolved misfit stress on the main slip plane is zero [67]. Thus, only secondary slip systems that are oblique to the basal plane can have a resolved misfit stress and may contribute to plastic relaxation. It has been observed that MDs following the secondary {11-23} {11-22} slip system can be generated at heterointerfaces when shear stress is intentionally or unintentionally induced by three-dimensional (3D) growth [68, 69], by crack formation [65, 70], or in close proximity to V-defects [71]. Therefore, the relaxation mechanism depends not only on the structure itself, but also on the growth conditions. In general, GaN/AlGaIn heterostructures grown under tensile stress on GaN substrates tend to crack along the {11-20} crystallographic direction at a certain critical thickness [70, 72, 73]. In the case of crack-free GaN/AlGaIn superlattices deposited under compressive strain, the main relaxation mechanism is the tilt of the *a*-type TDs towards {1-100}, the inclination angle depending on the lattice misfit between the MQWs and the underlayer [74]. It has been proposed that the diagonal movement is due to a staircase-like movement of the dislocations through the stack, with a misfit segment at each well. Strain relaxation via TD inclination has also been observed in AlGaIn layers deposited on mismatched AlGaIn [75].

In PAMBE growth, the metal-to-N ratio and the growth temperature are key parameters that define the strain relaxation rate during growth [76]. Ga-rich conditions delay crack propagation and minimize strain relaxation [58]. They also allow good control of the layer thickness and Al incorporation in AlGaIn alloys. In the case of GaN/AlN MQWs and in addition to the relaxation mechanisms described above, the periodic misfit relaxation appears associated with

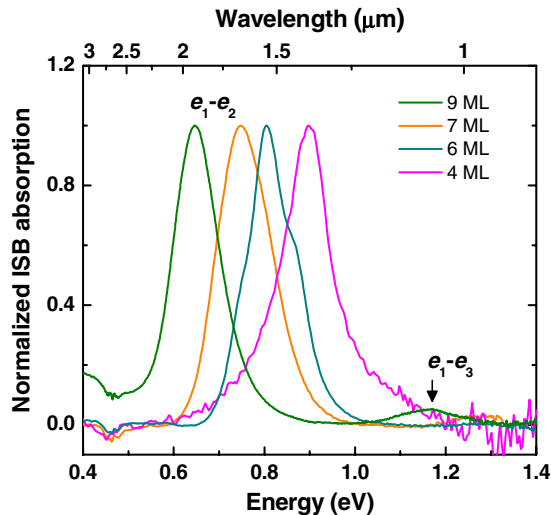


**Figure 3.** Room-temperature TM-polarized ISB absorption spectra from 20-period Si-doped GaN/AlN MQW structures with 3 nm thick AlN barriers and different GaN QW thickness. All the samples were grown on 1  $\mu\text{m}$  thick AlN-on-sapphire templates without cap layer. The absorption peaks labeled  $e_1-e_2$  and  $e_1-e_3$  are assigned to the corresponding intra-conduction-band transitions as described in figure 1(a). Reprinted with permission from [28]. Copyright 2008, American Institute of Physics.

the formation of stacking fault loops that initiate at the beginning of the AlN barrier deposition, propagate through the barrier and close within the following QW [58]. In contrast, transmission electron microscopy (TEM) images from GaN/AlGaIn superlattices (ternary alloy barriers) do not reveal stacking faults or other periodic defects [77].

**2.1.3. Intersubband optical characterization.** Figure 3 shows the ISB absorption of Si-doped AlN/GaN MQWs with 3 nm thick AlN barriers and QW thickness of 5, 6, 7 and 9 ML [14, 28]. The samples show a pronounced TM-polarized absorption, attributed to the transition from the first to the second electronic levels in the QW ( $e_1 \rightarrow e_2$ ), while no absorption was observed for TE-polarized light within experimental sensitivity. For large QWs ( $\geq 8$  ML), the  $e_1 \rightarrow e_3$  transition is observed, as indicated in figure 3; this transition is forbidden in symmetric QWs [78], but is allowed in nitride QWs because the internal electric field in the well breaks the symmetry of the potential. The experimental values of  $e_2-e_1$  and  $e_3-e_1$  as a function of the QW width are presented in figure 1, showing a good fit with theoretical calculations.

The line width of the absorption remains in the 70–100 meV range for QWs doped at  $5 \times 10^{19} \text{ cm}^{-2}$ , and the ISB absorption efficiency per reflection attains 3–5%. A record small line width of  $\sim 40$  meV has been achieved in non-intentionally doped structures [79]. The spectra present either Lorentzian shape or are structured with two or three well-defined Lorentzian-shaped peaks [14]. These multiple peaks correspond to the expected values of the  $e_1-h_1$  line in QWs whose thickness is equal to an integer number of GaN monolayers. For very narrow QWs, a variation in the thickness by 1 ML implies an important shift in the ISB transitions (about 100 meV for QWs of 4–5 ML). This value is comparable to

the full width at half maximum (FWHM) of the absorption lines, and hence results in well resolved PL peaks instead of broadening the emission lines. Thickness fluctuations might originate from a drift of the growth rate with time, resulting in a variation in the QW thickness. However, *in situ* measurements of the growth rate and TEM studies confirmed that structured absorption spectra appear in samples where no growth rate drift is detected. In these samples, cathodoluminescence studies confirmed the presence of in-plane thickness fluctuations which appear associated with dislocations or extended defects [28].

Regarding the thermal stability of the ISB transition in GaN/AlN MQWs, it has been found that the ISB absorption energy decreases only by  $\sim 6$  meV at 400  $^\circ\text{C}$  relative to its room temperature value [80].

Using GaN/AlN QWs, the  $e_2-e_1$  ISB transition can be tuned in the 1.0–3.5  $\mu\text{m}$  wavelength range by changing the QW thickness from 1 to 7 nm [14, 28, 35, 36, 38, 60, 73, 80, 81] with AlN barriers thicknesses in the 1.5–5.1 nm range. For larger QWs ( $> 5$  nm), the first two electron-confined levels get trapped in the triangular section of the QW, which results in a saturation of the  $e_2-e_1$  value. Therefore, to shift the absorption toward longer wavelengths, it is necessary to reduce the effect of the internal electric field in the QWs. A first approach consisted of using GaN/AlGaIn MQWs, thereby reducing the Al mole fraction in the barriers. By changing the geometry and composition, the ISB absorption can be tailored to cover the near-IR range above 1.0  $\mu\text{m}$  and mid-IR region up to 5.3  $\mu\text{m}$  [33, 34, 82–90]. To attain longer wavelengths, the requirement of substrate transparency imposes the replacement of sapphire-based templates by semi-insulating Si(1 1 1) as a substrate [21]. Using GaN-on-Si(1 1 1) templates, Kandaswamy *et al* have demonstrated the extension of the ISB absorption range of GaN/AlGaIn QWs up to 10  $\mu\text{m}$  [21], as illustrated in figure 4(a). A slight red shift of the ISB transition is observed when increasing the compressive strain in the QWs, as theoretically predicted [87].

To further reduce the ISB transition energy, Machhadani *et al* [91] propose an alternative strategy to approach a flat potential in the QW layers by engineering the internal electric field. The investigated structures contain a stack of step-QWs, each period consisting of a GaN well, an  $\text{Al}_{0.05}\text{Ga}_{0.95}\text{N}$  step barrier and an  $\text{Al}_{0.1}\text{Ga}_{0.9}\text{N}$  barrier. Transmission measurements performed at 4 K reveal TM-polarized ISB absorption at  $\sim 2$  THz, in good agreement with simulations, as shown in figure 5.

**2.1.4. Effect of doping.** In order to observe ISB absorption, it is necessary to control the carrier concentration in the QWs to guarantee that the first electronic level is populated. High doping levels also have an effect on the targeted operating wavelength. The ISB absorption energy can blue shift markedly due to many-body effects [22, 38], mostly due to exchange interaction and depolarization shift, as illustrated in figures 4(b) and (c). On the other hand, studies of the effect of the dopant location have shown a dramatic reduction of the ISB absorption line width by using a  $\delta$ -doping technique with Si donors placed at the end of the QW [92]. This line width



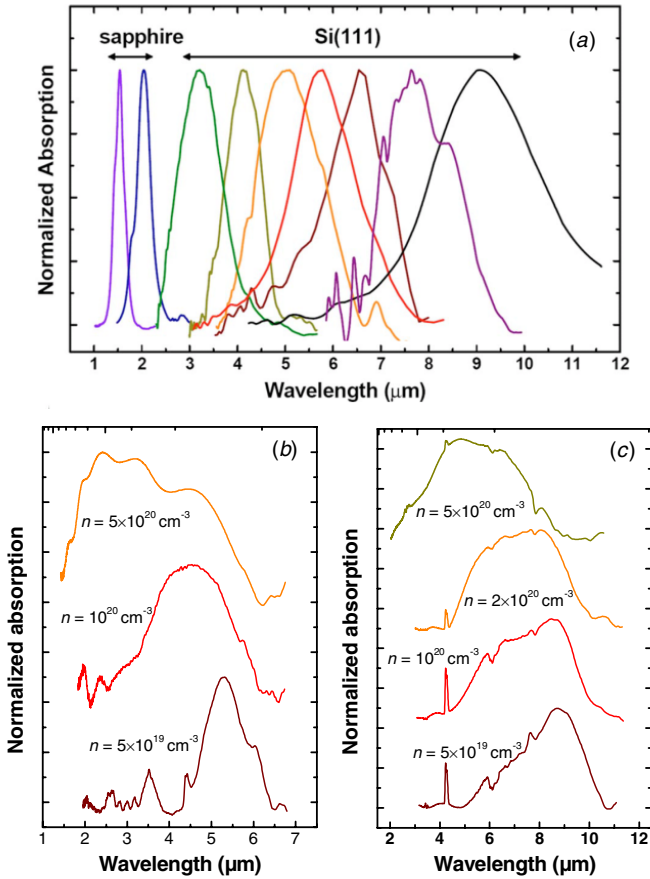


**Figure 4.** (a) Room-temperature TM-polarized IR photo-induced absorption spectra measured in GaN/AlGaIn MQW structures with different barrier Al contents and QW width, grown either on sapphire or on Si(111) templates. Reprinted with permission from [21]. Copyright 2009, American Institute of Physics. (b) Infrared absorption spectra for TM-polarized light measured from GaN/Al<sub>0.2</sub>Ga<sub>0.8</sub>N (3 nm/3 nm) MQWs with different doping levels. Spectra are vertically shifted for clarity. Reprinted with permission from [22]. Copyright 2010, American Institute of Physics. (c) IR absorption spectra for TM-polarized light measured from GaN/Al<sub>0.1</sub>Ga<sub>0.9</sub>N (7 nm/4 nm) MQWs with different doping levels. Spectra are vertically shifted for clarity. (After [22].)

reduction is attributed to an improvement of the interfacial roughness.

When integrating III-nitride nanostructures in a complete device, it is necessary to keep in mind that the magnitude of the carrier distribution depends not only on the Si doping level in the QWs, but also on the presence of non-intentional dopants, and on the carrier redistribution due to the internal electric field. The large polarization discontinuities in the III-N material system can result in a significant (even dominant) contribution to the IR absorption in GaN/AlN superlattices [28].

## 2.2. Coupled quantum wells

The design of advanced ISB devices, like optically or electrically pumped ISB lasers, requires the exploitation of multi-level system with finely tuned oscillator strengths and lifetimes. Coupled QWs are the basic element for such systems. In III-nitrides, the realization of coupled QWs is complicated by the relatively heavy electron effective mass

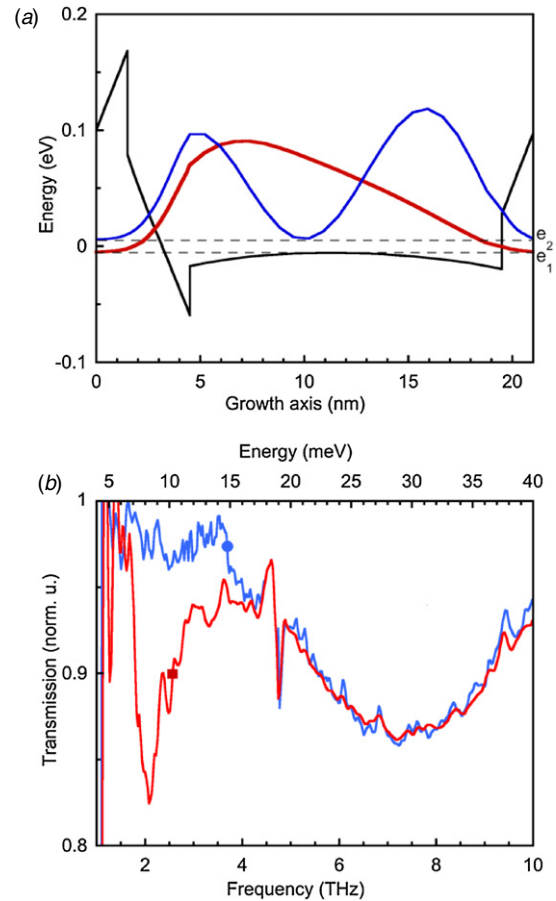


**Figure 5.** (a) Conduction band profile and squared envelope functions of the first two electronic levels ( $e_1$ ,  $e_2$ ) for a step-QW sample with 15 nm thick step barrier. (b) Transmission spectra for TM- (square) and TE- (circle) polarized light at  $T = 4.7$  K. Reprinted with permission from [91]. Copyright 2010, American Institute of Physics.

and the large conduction band offset. As a result, very thin barriers (1–3 ML) are required to achieve strong interwell coupling in the GaN/AlN material system [93].

Coupling between GaN QWs was first experimentally investigated by Gmachl *et al* [34, 37] by using double GaN QWs coupled by AlGaIn barriers with large (0.65 or 0.9) Al mole fractions. The coupling barrier thicknesses varied from 0.7 to 6 nm. Degenerate doping of the QWs ( $10^{20} \text{ cm}^{-3}$ ) was used to establish a common reference energy at the Fermi level, which decreases the uncertainties related to intrinsic internal electric fields. The broadening and structuration of the ISB absorption peaks were attributed to transitions toward excited states exhibiting anticrossing.

Coupled GaN/AlN QWs were first demonstrated by Tchernycheva *et al* [94] using 0.5 nm thick AlN coupling barriers. The intersubband absorption spectra present two distinct peaks attributed to the transition, firstly between the ground states of the two coupled wells, and secondly between the ground state and the delocalized excited state between the two wells. As an alternative approach, Driscoll *et al* have opted to decrease the Al content of the coupling barrier to 39–53%, so that strong coupling is achieved with thicker barriers ( $\sim 5$  ML). In this fashion, the barrier's Al content



can be used as a tunable parameter to control the coupling strength [95].

The influence of polarization-induced electric fields on the ISB absorption and the associated variation of the refractive index in AlN/GaN coupled QWs has been theoretically analyzed by Cen *et al* [96, 97] using a self-consistent Schrödinger–Poisson solver. The results are used to discuss the application of these structures in ultrafast two-color optoelectronic devices and electro-optical modulators operating within the optical communication wavelength range.

### 2.3. In containing superlattices: AlInN/GaN, AlInN/GaInN and GaN/GaInN

As described above, the lattice mismatch between GaN and AlN can lead to high defect densities and risk of cracking in GaN/AlN superlattices. An alternative material approach to overcome this problem is the use of AlInN alloys. AlInN with an In composition around 17–18% is lattice matched to GaN and presents a refractive index contrast equivalent to AlGaIn with 46% Al content (6% contrast with GaN at 1.55  $\mu\text{m}$  wavelength). Therefore, AlInN is a promising material to form distributed Bragg reflectors and thick waveguide layers [98]. However, lattice-matched AlInN/GaN heterostructures still exhibit an electric field as large as 3 MV cm<sup>-1</sup>, solely generated by the spontaneous polarization discontinuity.

The potential of AlInN/GaN lattice-matched systems for application in ISB technology has been explored [99, 100]. However, this material system is not adapted to serve as active region for telecommunication devices since the conduction band offset is in the range of  $\sim 1$  eV [101]. Nevertheless, ISB absorption in the near-IR spectral region has been reported at 2.3–2.9  $\mu\text{m}$  in lattice-matched GaN/AlInN superlattices grown by MOVPE [99] and by MBE [102].

An alternative approach to manage the strain in the structure while retaining access to shorter wavelengths is possible by adding small concentrations of In (below 10%) both in the barrier and in the QW, forming an AlInN/GaInN superlattice [103, 104]. This material combination reduces the probability of crack propagation in comparison to GaN/AlN, although it maintains a certain degree of strain. Room-temperature ISB absorption in the 1.52–2.45  $\mu\text{m}$  wavelength range has been demonstrated in AlInN/GaInN MQWs [103]. Efforts to simulate the electronic structure of these superlattices have been recently reported [105]; however, it remains challenging to control precisely the In mole fraction during the superlattice growth.

Regarding the GaN/GaInN system, only theoretical calculations of the ISB transition energy have been published so far [106].

### 2.4. Quantum dots

An alternative approach to QW structures for the fabrication of devices is based on optical transitions between bound states in the conduction band of quantum dot (QD) superlattices [107, 108]. Quantum dot IR photodetectors (QDIPs) are expected to ultimately outperform QWIPs in terms of low dark current, high photoelectric gain and sensitivity [109].

Furthermore, under certain conditions, intraband bound-to-continuum transitions in QDs can be nearly independent of the polarization of excitation [110–112].

In the case of III-nitrides, GaN/AlN QD structures can be synthesized by PAMBE through GaN deposition under compressive strain and under N-rich conditions [79, 113]. In this situation, 2D growth proceeds normally to create a 2-ML-thick wetting layer. Due to the lattice mismatch between AlN and GaN, further GaN deposition leads to the formation of 3D islands above this 2D wetting layer (Stranski–Krastanov growth mode). These GaN QDs are well-defined hexagonal truncated pyramids with {1–103} facets [114], and no Ga–Al interdiffusion has been observed [115]. The QD size can be tuned by modifying the amount of GaN in the QDs, the growth temperature or the growth interruption time after deposition of the QDs (Ostwald ripening). By adjusting the growth conditions, QDs with height (diameter) in the range of 1–1.5 nm (10–40 nm), and density between 10<sup>11</sup> cm<sup>-2</sup> and 10<sup>12</sup> cm<sup>-2</sup> can be synthesized (see atomic force microscopy image in figure 6(a) as an example) [116]. To populate the first electronic level, silicon can be incorporated into the QDs without significant perturbation of the QD morphology.

Similar GaN/AlN QDs can be synthesized by ammonia-MBE by performing a growth interruption after deposition of a GaN thickness larger than 3 ML ( $\sim 0.8$  nm), which instantaneously leads to the formation of 3D islands [117]. Regarding MOVPE, the formation of 3D GaN islands has been first demonstrated using Si as an antisurfactant [118]. With this method, the shape and the density of GaN QDs can be controlled by the Si dose, the growth temperature, the growth time and the Al content of the AlGaIn layer below the islands [119]. GaN/AlN QDs have also been synthesized by low-pressure MOVPE using very low V/III ratios [120]. Depositing over a critical thickness of 4 ML of GaN results in a spontaneous transition from the 2D to the 3D growth mode. The density of the QDs can be tuned between 10<sup>9</sup> and 10<sup>10</sup> cm<sup>-2</sup>, keeping typical QD diameter and height around 20 and 2 nm, respectively. The size of the QDs can be controlled to a considerable extent by changing the growth temperature and V/III ratio.

Andreev *et al* have calculated the electronic structure of GaN/AlN QDs using the  $k \times p$  model and taking the internal electric field into account [121–123]. These calculations have been complemented by Ranjan *et al* [124] through the use of the tight-binding theory and a self-consistent treatment to account for carrier screening of the electric field. The models show that the polarization-related internal electric field localizes the electrons at the pyramid apex, whereas the holes are located close to the wetting layer. In addition to the carrier separation along the growth axis, the electric field can provide a strong additional lateral confinement for carriers localized in the dot, which greatly modifies their electronic structure and optical properties [123].

From the experimental viewpoint, early studies of intraband phenomena in GaN QDs showed photoinduced IR absorption in the 1.27–2.4  $\mu\text{m}$  spectral range in undoped nanostructures synthesized by ammonia-MBE [125]. Later on, PAMBE-grown Si-doped QD superlattices have been reported

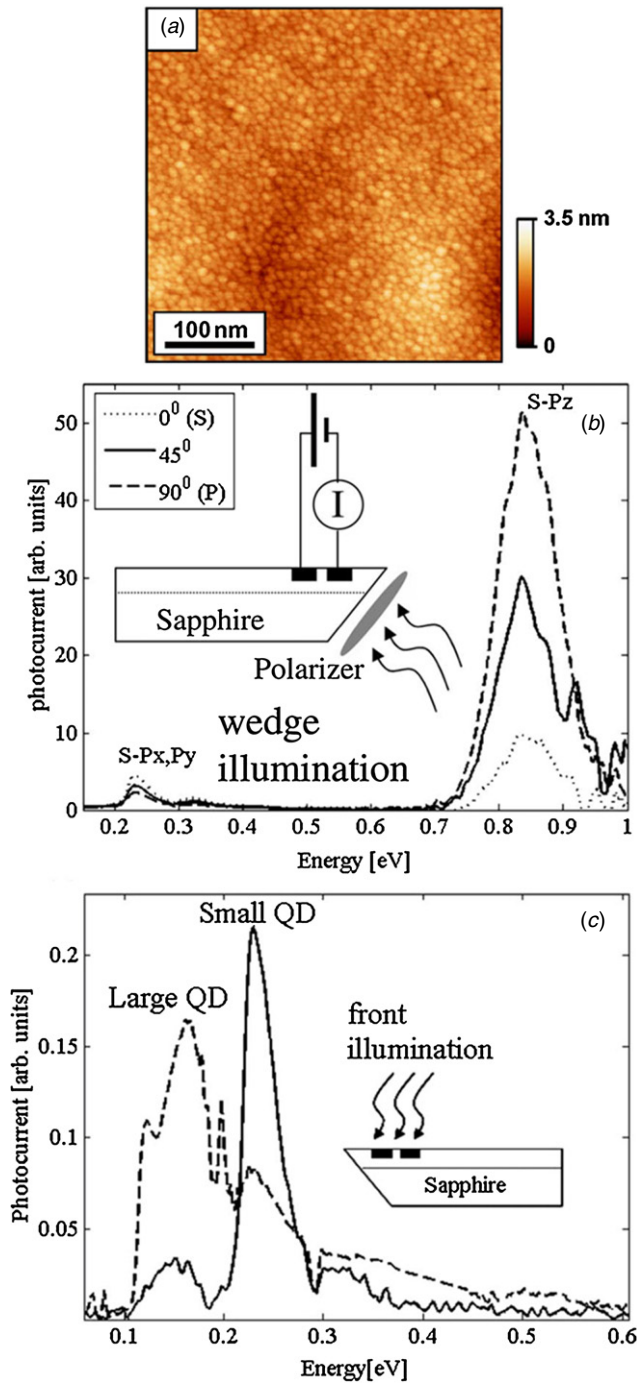


**Figure 6.** (a) Atomic force microscopy image of a GaN QD layer synthesized on AlN by PAMBE, showing a high density ( $\sim 10^{12} \text{ cm}^{-2}$ ) of small (height  $\sim 1.3 \text{ nm}$ ; base diameter  $\sim 11 \text{ nm}$ ) QDs. (b) Polarization-dependent spectral response (photocurrent) of a GaN/AlN QD stack measured in wedge illumination. The normalized response of both  $s-p_z$  in the near IR and  $s-p_{x,y}$  in the mid-IR; the  $s-p_z$  peak is about ten times larger than the  $s-p_{x,y}$  peak. (c) Mid-IR spectral response of two GaN/AlN QD stacks with smaller (full line) and larger (dash line) QDs measured at  $T = 12 \text{ K}$  under front illumination and 10 V bias. Sapphire cutoff is at 0.22 eV. Reprinted with permission from [127]. Copyright 2009, American Physical Society.

to exhibit strong TM-polarized intraband absorption at room temperature, which can be tuned from 0.74 eV ( $1.68 \mu\text{m}$ ) to 0.90 eV ( $1.38 \mu\text{m}$ ) as a function of the QD size [116, 126]. The

broadening of the absorption peak can be as small as  $\sim 80 \text{ meV}$  for the most homogeneous samples. This absorption line is attributed to transitions from the ground state of the conduction band,  $s$ , to the first excited electronic state confined along the growth axis,  $p_z$ . The lateral confinement in the QDs should give rise to additional transitions under TE-polarized excitation. However, taking into account the lateral dimension of the QDs  $\sim 7 \text{ nm}$ , the  $s-p_{x,y}$  transitions should be masked by the sapphire absorption for  $\lambda > 5 \mu\text{m}$ . The optical signature associated with  $s-p_{x,y}$  was first observed by Vardi *et al* who studied mid-IR intraband transitions in GaN/AlN QDs using in-plane electronic transport at low temperatures [127], as illustrated in figures 6(b), (c). The measured  $s-p_{x,y}$  energy separation (0.1–0.3 eV) presented in figure 6(c) was significantly larger than the equivalent transition energy in InGaAs/GaAs QDs. Their analysis shows that the appearance of large energy  $s-p_{x,y}$  in GaN/AlN QDs is due to the strong internal electric field in the QDs which results in stronger confinement of the electrons at the QD top facet.

The homogeneous line width of the  $s-p_z$  intraband transition at  $1.55 \mu\text{m}$  in GaN/AlN QDs was assessed by means of nonlinear spectral hole-burning experiments [128]. These measurements demonstrated that electron–electron scattering plays a minor role in the coherence relaxation dynamics, since the homogeneous line width of 15 meV at 5 K does not depend on the incident pump power. This suggests the predominance of other dephasing mechanisms such as spectral diffusion.

TM-polarized IR absorption in the  $1.6\text{--}2 \mu\text{m}$  wavelength range, attributed to  $s-p_z$  intraband transitions, has also been reported in ternary AlGaIn/AlN QDs measured at room temperature. The  $s-p_z$  transition red shifts for increasing Al mole fraction in the QDs as a result of the reduction of the band offset, in good agreement with theoretical calculations [129].

## 2.5. Alternative crystallographic orientations

The already high design complexity of ISB devices further increases in materials with internal electric field like polar III-nitrides. A simple solution to this problem consists in using non-polar crystallographic orientations like the  $m$ -plane  $\{1\bar{1}00\}$  or the  $a$ -plane  $\{11\bar{2}0\}$  [130]. However, epitaxy for these orientations is an arduous task, due to strong anisotropy of the surface properties, resulting in a high density of crystalline defects. An alternative approach is the growth on semipolar planes [130], which are those  $(hki\bar{l})$  planes with at least two non-zero  $h$ ,  $k$  or  $i$  Miller indices and a nonzero  $l$  Miller index. Semipolar planes allow a considerable reduction in the internal electric field [131] while presenting a lower in-plane anisotropy than non-polar surfaces [132, 133].

Regarding nonpolar materials, ISB optical absorption at  $\lambda \sim 2.1 \mu\text{m}$  with a FWHM = 120 meV has been reported in Si-doped 1.75 nm thick GaN QWs with 5.1 nm thick AlN barriers grown by PAMBE on  $r$ -plane sapphire and displaying pure  $a$ -plane orientation [134].

Near-IR ISB absorption has also been reported on semipolar  $(11\bar{2}2)$ -oriented GaN/AlN MQWs grown by PAMBE [133]. The band structure of these semipolar

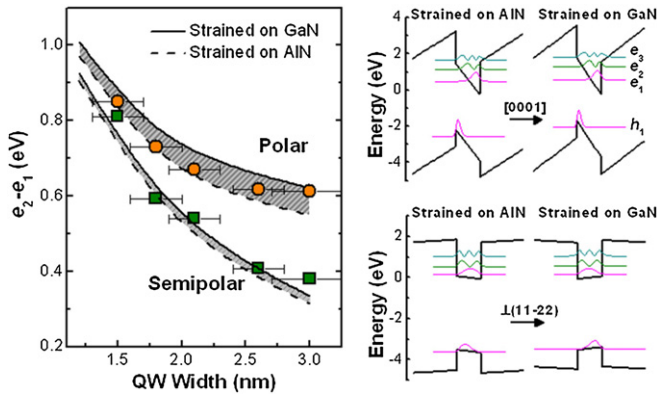


**Figure 7.** Left: Variation of  $e_2 - e_1$  energy as a function of well width in polar and semipolar GaN/AlN MQWs with 5 nm thick AlN barriers, strained on GaN and AlN. Right: band diagram of (0001)- and (11-22)-oriented GaN/AlN (2.5 nm/5 nm) MQWs, assuming the structure fully strained on AlN and on GaN. Adapted with permission from [133]. Copyright 2008, American Institute of Physics.

GaN/AlN QWs strained on GaN and on AlN is represented in figure 7. In comparison to polar QWs, semipolar structures exhibit quasi-square potential band profiles with symmetric wavefunctions, due to the reduced electric field in the range of  $0.5\text{--}0.6\text{ MV cm}^{-1}$  in the QWs. The evolution of the  $e_2 - e_1$  ISB transition energy with the QW thickness is represented in figure 7, where symbols correspond to experimental measurements obtained from identical polar and semipolar samples consisting of 40 periods of GaN/AlN with 3 nm thick AlN barriers. The absorption FWHM ( $\sim 80\text{--}110\text{ meV}$  [133]) is comparable to the one measured in polar structures [14, 28]. However, in semipolar structures, the reduction in the internal electric field results in a red shift of the ISB energy. Also the spectral shape of semipolar absorption is Gaussian, in contrast to the Lorentzian shape described for polar GaN/AlN QWs. This is due to the spectral dispersion generated by thickness fluctuations and by the presence of stacking faults in semipolar material, both inducing carrier localization in the range of a few meV, much smaller than the FWHM of the ISB absorption line.

Another approach to eliminate the internal electrical field in III-nitride heterostructures is the use of III-nitride semiconductors crystallized in the zinc-blend crystallographic phase. The LO phonon energy in cubic GaN is almost the same as in wurtzite GaN ( $92.7\text{ meV}$  [135]), but the effective mass is significantly smaller ( $m^* = 0.11\text{--}0.17m_0$  [136, 137]) than in wurtzite GaN ( $m^* = 0.2m_0$ ), which should result in higher gain and lower threshold current in QCLs. The cubic orientation can be selected by PAMBE using 3C-SiC substrates. However, due to their thermodynamically unstable nature, cubic films present low structural quality with a high density of stacking faults. ISB absorption in the  $1.40\text{--}4.0\text{ }\mu\text{m}$  spectral range has been reported in cubic GaN/AlN MQWs [138, 139], in agreement with theoretical calculations assuming a conduction band offset of  $1.2\text{ eV}$  and an effective mass  $m^* = 0.11m_0$  (see figure 8). ISB THz absorption at  $4.7\text{ THz}$  has also been observed in cubic GaN/ $\text{Al}_{0.05}\text{Ga}_{0.95}\text{N}$  (12 nm/15 nm) QWs [139].

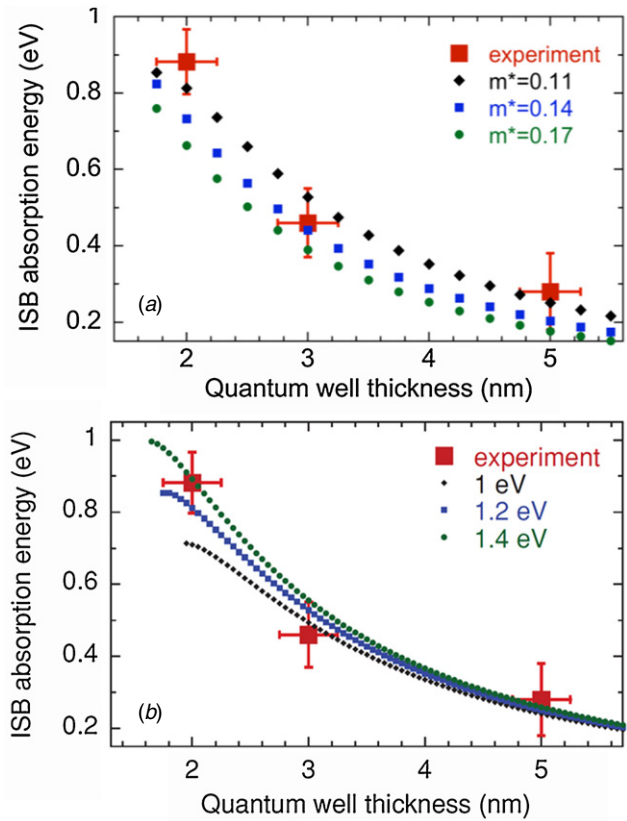


**Figure 8.** (a) ISB transition energy in cubic GaN/AlN MQWs calculated within effective mass approximation compared to the experimental data (red squares). The following parameters are used in the calculations: conduction band offset =  $1.2\text{ eV}$  for all curves; black diamonds:  $m_{\text{eGa}}^* = 0.11m_0$ ,  $m_{\text{hhGa}}^* = 0.8m_0$ ,  $m_{\text{eAlN}}^* = 0.19m_0$ ,  $m_{\text{hhAlN}}^* = 1.2m_0$ ; blue squares:  $m_{\text{eGa}}^* = 0.14m_0$ ,  $m_{\text{hhGa}}^* = 0.86m_0$ ,  $m_{\text{eAlN}}^* = 0.28m_0$ ,  $m_{\text{hhAlN}}^* = 1.44m_0$ ; green circles:  $m_{\text{eGa}}^* = 0.17m_0$ ,  $m_{\text{hhGa}}^* = 0.85m_0$ ,  $m_{\text{eAlN}}^* = 0.3m_0$ ,  $m_{\text{hhAlN}}^* = 1.39m_0$ . (b) ISB absorption energies calculated for different conduction band offset values, compared to the experimental data (red squares). The following effective masses are used:  $m_{\text{eGa}}^* = 0.11m_0$ ,  $m_{\text{hhGa}}^* = 0.8m_0$ ,  $m_{\text{eAlN}}^* = 0.19m_0$ , and  $m_{\text{hhAlN}}^* = 1.2m_0$ . In both plots, the error bars correspond to  $\pm 1\text{ ML}$  thickness fluctuation for the abscissa and to the FWHM of the transition for the ordinate. Reprinted with permission from [139]. Copyright 2009, American Physical Society.

### 3. All-optical switches

The development of multi-terabit optical time division multiplexing (OTDM) networks depends on the implementation of all-optical switches and wavelength converters operating at room temperature. In these devices, the switching is based on ISB absorption bleaching by an intense control pulse, as originally demonstrated at long IR wavelengths using GaAs/AlGaAs [140]. These devices should demonstrate an ultrafast response capable of sustaining high repetition rates with low switching energy and high contrast ratio. Attempts to realize these features lead to the consideration of resonant nonlinearities in semiconductor nanostructures [141]. Thanks to the ultrafast ISB recovery time (in the  $140\text{--}400\text{ fs}$  range [37, 142–146]) associated with the strong interaction of electrons with LO phonons, GaN/AlN QWs or QDs have been proposed as the active medium for



all-optical switches (saturable absorbers) operating at Tbit/s data rates and at telecommunication wavelengths.

The use of GaN/AlGaIn QWs for all-optical modulators at telecommunication wavelengths was first proposed by Suzuki *et al* [15, 147]. Since then, all-optical switching at  $\sim 1.55 \mu\text{m}$  with sub-picosecond commutation time has been demonstrated by several groups [31, 64, 144, 145, 148–151]. In general, these devices consist of GaN/AlN MQWs embedded in a ridge waveguide. In such structures, a critical parameter to reduce transmission losses is the reduction of edge-type dislocations. These defects introduce acceptor centers where electrons can be captured, and therefore can effectively act as a wire-grid polarizer which leads to selective attenuation of the TM-polarized signal [152]. Control switching energies as low as 38 pJ for 10 dB modulation depth [149] and 25 pJ for 5 dB contrast [151] have been demonstrated using a waveguide with an AlN cladding below the active GaN/AlN QWs, and GaN or  $\text{Si}_x\text{N}_y$  as the upper cladding layer, respectively. Theoretical calculations predict a reduction of the switching energy by a factor of 30 by replacing the GaN/AlN QWs with properly designed AlN/GaN/AlGaIn coupled QWs [153, 154].

From the material viewpoint, the parameter responsible for absorption saturation is the optical third-order susceptibility,  $\chi^{(3)}$ . Comparative studies using the forward degenerate four-wave mixing technique in a boxcars configuration point to an increase of  $\chi^{(3)}$  by a factor of 5 in QDs compared to QWs [155]. From the experimental viewpoint, the intraband absorption saturation of GaN/AlN QDs has been probed by Nevou *et al* [31], obtaining values in the range of  $15\text{--}137 \text{ MW cm}^{-2}$  ( $0.03\text{--}0.27 \text{ pJ } \mu\text{m}^{-2}$ ). In spite of the large signal variation (a consequence of the focusing uncertainty in the sample), even the upper estimate of the saturation intensity for QDs is smaller than the corresponding value for GaN/AlN QWs ( $9.46 \text{ W } \mu\text{m}^{-2}$  [149]).

## 4. Resonant tunneling transport

### 4.1. Mesa-structured resonant tunneling diodes

Understanding electron resonant transport is of critical importance for the fabrication of electrically driven ISB devices. Furthermore, resonant tunneling diodes (RTDs) are attractive for terahertz frequency applications, since oscillators based on RTDs have recently shown operation frequencies up to 1.1 THz [156, 157]. III-N heterostructures in particular are expected to provide a larger peak-to-valley ratio (PVR) in the resonant tunneling current due to their large and adjustable band offsets compared to other materials.

Studies of electron transport through single GaN/AlN/GaN barriers indicate that bias induces a redistribution of charges in the GaN layers, but does not significantly modify the polarization-induced electric field in the barrier [158, 159]. For 0.5 and 1 nm thick AlN barriers, electron tunneling is confirmed by optical characterization. For AlN barriers in the 1–3 nm range, conductive AFM measurements reveal efficient current blockage, with pure screw dislocations being the main source of leakage current [159, 160]. Finally, leakage due to AlN relaxation and interband tunneling was observed for 5 nm thick barriers [159, 161].

The first theoretical investigation into resonant tunneling in GaN/AlGaIn double-barrier heterostructures was presented in 2001 by Grinyaev and Ruzzhuvalov [162]. Since then, the development of a nitride-based RTD became a hot topic. First reports of resonant tunneling in Al(Ga)N/GaN double barriers [163–166] were highly controversial because of the scarcity and irreproducibility of the published data. In 2002, Kikuchi *et al* reported the first measurements of resonant tunneling in PAMBE-grown AlN/GaN heterostructures consisting of  $40 \mu\text{m}$  square encapsulated mesa-diodes [163]. A negative differential resistance (NDR) was recorded at 2.4 V bias, with a peak current density of  $180 \text{ A cm}^{-2}$  and PVR of 32. However, the NDR was only observed in forward bias<sup>1</sup> and only when scanning from negative toward positive bias. Theoretical calculations accounting for polarization effects [167–171] can explain some of the features observed by Kikuchi, namely the asymmetric current–voltage characteristics, but not the current hysteresis. Since then, many other groups have faced similar problems of hysteresis and instabilities [159, 172–178].

The development of III-N RTDs still remains a challenging task due to the presence of trap-like defects and impurities in the heterostructures. These traps are thermally activated, and therefore their effect on the tunneling current is minimized when the temperature decreases [179], resulting in a larger PVR at lower temperatures. Improved reproducibility of the NDR is achieved by decreasing the substrate dislocation density [173, 175, 176], decreasing the device mesa size [159, 180], or using low-aluminum-content AlGaIn/GaN double-barriers [178]. The NDR reproducibility is also drastically improved when scanning the voltage from a sufficiently negative starting bias due to the detrapping of charges via the Poole–Frenkel effect [159, 180].

Resonant electron transport through MQWs, namely a seven-period GaN/AlN stack, has also been reported [181]. The devices show asymmetric current–voltage characteristics displaying NDR features at room temperature under forward bias. These features, which persist for multiple scans and are reproducible for both upward and downward sweeping voltage, are interpreted as a consequence of the resonant tunneling between the fundamental and excited states of adjacent QWs.

### 4.2. Resonant tunneling transport in nanowires

III-Nitride nanowire (NW) heterostructures offer an alternative approach by minimizing the effects of strain relaxation, which not only provides dislocation-free material, but also attenuates the piezoelectric effects. Nano-scale RTDs based on NW heterostructures were first demonstrated using InP/InAs [182]. Recently, electron resonant tunneling transport was presented in single defect-free *n-i-n* GaN NWs containing closely spaced (4 nm) AlN double barriers grown by PAMBE [183], as illustrated by the TEM image in figure 9(a). The devices were fabricated with a back-gate NW-field effect transistor geometry, placing the double-barrier structure in between the source and drain contacts. The transistor's low-temperature

<sup>1</sup> It is conventionally considered that the positive electrode is the top contact in samples grown along the [000 1] axis.



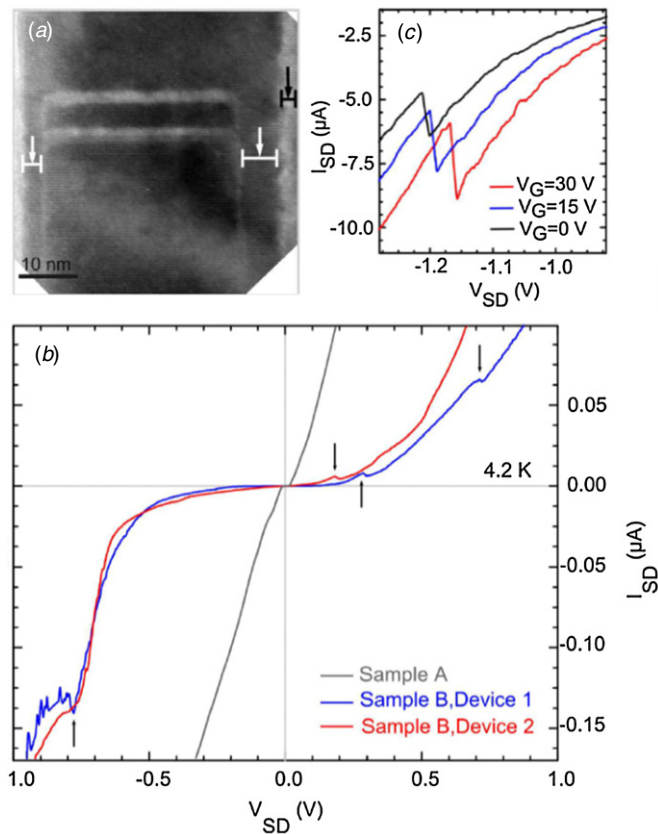


**Figure 9.** (a) High-resolution TEM image a GaN NW section containing a double-barrier heterostructure, i.e. a pair 2 nm thick AIN barriers (bright contrast) separated by a 6 nm thick GaN section. The GaN lateral growth around the AIN barriers is resolved in the image (white arrows). The sharp contrast observed at the right facet of the NW (black arrow) corresponds to native gallium oxide. (b) Source-drain current–voltage ( $I_{SD} - V_{SD}$ ) characteristics at 4.2 K of GaN NWs with two closely-spaced AIN tunnel barriers in comparison with that of *n-i-n* GaN NWs. (c)  $I_{SD} - V_{SD}$  characteristics showing the evolution of the NDR appearing at negative  $V_{SD}$  for different values of gate voltage  $V_G$ . Adapted with permission from [183]. Copyright 2010, American Chemical Society.

current–voltage characteristics (figure 9(b)) exhibit NDR features, attributed to the onset of tunneling via the confined levels between the AIN barriers. The bias value displaying NDR features can be tuned by adjusting the electrostatic potential via the back-gate bias (figure 9(c)). The NDR features in these NW-RTDs are reproducible for both bias sweeping directions and no degradation of the device characteristics are found after repeated measurements.

Rigutti *et al* studied the electrical transport through GaN NWs containing multiple GaN/AIN nano-disks [184]. They found that the presence of a spontaneously formed GaN shell surrounding GaN/AIN nano-disks significantly influences the device characteristics. When the GaN shell does not exist, the current mainly flows through the multiple nano-disks and reproducible NDR is observed, which is attributed to the electron tunneling through the electronic states available in those nano-disks. In contrast, the NDR feature disappears when the GaN shell is present, as the current mainly flows through the shell close to the NW sidewalls.

Finally, there has been an attempt to take advantage of the suppressed internal electric field in AIN/GaN heterostructures grown in the non-polar orientation by growing the AIN/GaN double barriers on the *m*-plane sidewall of a GaN NW [185]. The electron transport was measured using an SEM equipped with nano-manipulators, capable of contacting individual NWs. NDR characteristics were found in the ensemble and individual AIN/GaN core shell NWs, and are explained by the resonant tunneling through the AIN/GaN double barrier. Individual NW measurements show NDR at room temperature with a peak current density of  $5 \times 10^5 \text{ A cm}^{-2}$ .

## 5. Electro-optical modulators

Electro-optical modulators are essential components for fiber-optic communication at  $\lambda = 1.55 \mu\text{m}$ , since they aid to overcome the inherent speed limitations and positive chirp of conventionally used interband semiconductor lasers. Electro-optical amplitude and phase modulators allow for control of the amplitude, phase and/or polarization state of an optical beam as a function of a bias voltage. State-of-the-art technologies in this field include modulators based on the QCSE of interband transitions in InGaAsP QWs [186], and others based on the electro-optic effect in materials like LiNbO<sub>3</sub> within a Mach–Zehnder configuration [187]. These devices present several drawbacks, such as low saturation power and positive chirp in the former case, and the need for high driving voltage and larger size in the latter case. Achieving a significant improvement in device performance requires a change of technological approach. Exploiting ISB transitions in QWs has been proposed as a means to reduce the driving voltage and increase the bandwidth [188–190]. Moreover, the higher ISB transitional oscillator strength in comparison to interband transitions, should allow for further miniaturization of the devices.

The first electro-absorption ISB modulation experiments on AIN/GaN QWs were based on the electrical depletion of a five-period AIN/GaN (1.5 nm/1.5 nm) MQW structure grown on a thick GaN buffer [191]. The absorption spectrum of such a sample presents two distinct peaks related to ISB transitions in both the QWs and in the 2D electron gas located at the interface of the lowest AIN barrier and the underlying GaN buffer. The ratio of these two absorption peaks can be adjusted by applying an external field, which influences the overall band structure and, more specifically, the free carrier density in the QWs. To increase the modulation depth, the interaction of light with the active medium should be enhanced, which can be achieved with a waveguide geometry [17]. Through the use of a 1- $\mu\text{m}$ -thick Al<sub>0.5</sub>Ga<sub>0.5</sub>N waveguiding layer on AIN, and with three active GaN/AIN QWs operating at  $\lambda = 1.55 \mu\text{m}$ , a modulation depth of 13.5 dB was observed for a  $-9\text{V}/+7\text{V}$  voltage swing (10 dB for 5 V voltage swing).

The intrinsic speed limit can be greatly improved by emptying active QWs into a local reservoir, instead of transferring carriers over the whole active region. This is the principle of the coupled-QW modulator: The electro-modulation originates from electron tunneling between a wide well (reservoir) and a narrow well separated by an

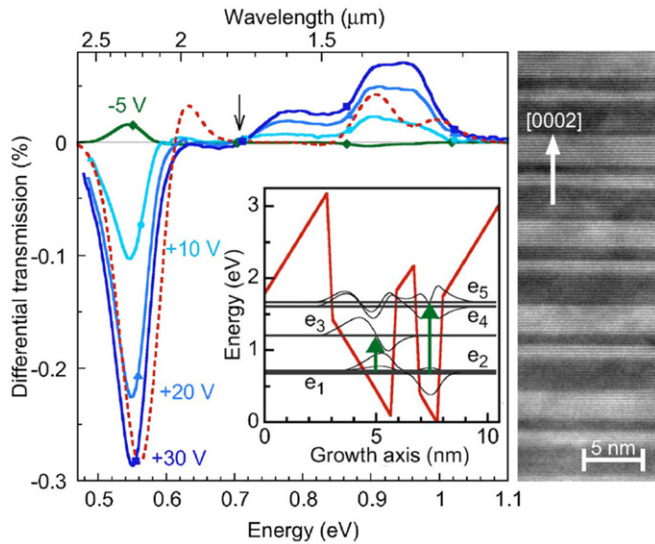


**Figure 10.** Differential transmission  $\Delta T/T$  for applied bias pulses of +30 V (squares), +20 V (triangles), +10 V (circles), and -5 V (diamonds). The arrow points the energy at which a discontinuity of the derivative of the FTIR spectrum occurs. The dashed line shows the calculated transmission change for 0.8 V bias across the active region. The inset shows the conduction band profile and energy levels for one period of coupled QWs. Right panel: high-resolution TEM image showing five periods of coupled QWs in the active region. Adapted with permission from [192]. Copyright 2007, American Institute of Physics.

ultrathin ( $\sim 1$  nm) AlN barrier (see the inset of figure 10). Experiments on GaN QW coupling via AlN [94] or AlGaIn [95] barriers have set the basis for the demonstration of room-temperature ISB electro-modulated absorption at telecommunication wavelengths in GaN/AIn coupled QWs with AlGaIn contact layers [192–194]. Figure 10 illustrates the design and performance of a modulator with 1 nm thick AlN coupling barriers [192, 193]. Positive bias favors electron transfer from the reservoir well to the active well, which increases the ISB absorption at 1.3–1.6  $\mu\text{m}$ . Under reverse bias, the electrons tunnel back to the reservoir well and the structure becomes transparent at telecommunication wavelengths. The  $BW_{-3\text{dB}}$  cut-off frequency is limited by the resistance  $\times$  capacitance ( $RC$ ) time constant and is as high as 3 GHz for  $15 \times 15 \mu\text{m}^2$  mesas. This frequency could be further improved by reducing the access resistance of the AlGaIn contact layers. According to Hölmstrom, the high-speed performance of such modulators will ultimately be determined by the ISB absorption line width  $\Gamma$ , since their capacitance depends on the line width as  $C \sim \Gamma^3$  [188, 189].

All the above-described electro-optical modulators rely on light amplitude modulation via ISB absorption. Based on Kramers–Kronig relations, the ISB absorption should also translate into a variation of the refractive index at wavelengths close to the transition, which can be used for phase modulation. This concept was verified experimentally at mid-IR ( $\sim 10 \mu\text{m}$ ) wavelengths using the stark shift of ISB transitions in GaAs/AlGaAs step QWs [195]. The strongly nonlinear susceptibility observed in GaN/AIn QWs [155, 196] has led to the first theoretical proposals of all-optical cross-phase modulators [96].

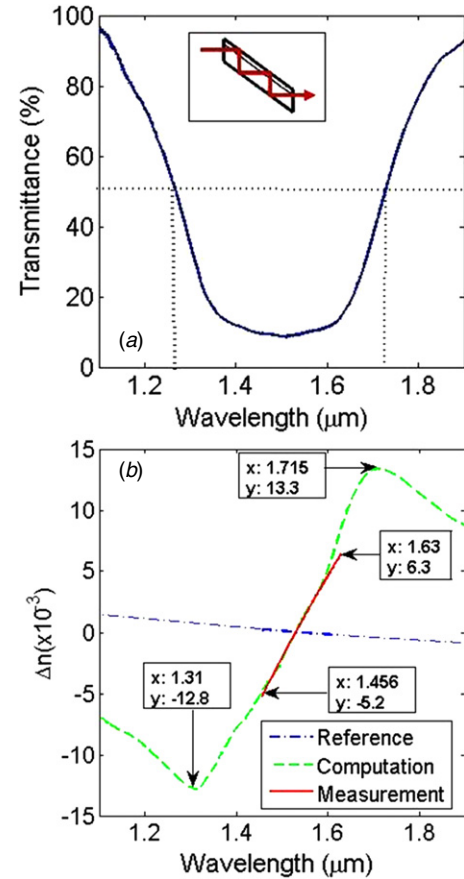


**Figure 11.** (a) Normalized transmittance of 100 periods of GaN/AIn QWs measured in multi-pass waveguide configuration as described in the inset. (b) Measured refractive index dispersion due to ISB absorption in the GaN/AIn MQWs interaction layer (solid red line). Kramers–Kronig computation of the FTIR measured absorption shown on the left (green dashed line). The measured reference sample refractive index dispersion (blue dotted-dashed line) is of the order of  $10^{-4}$ . (Adapted from [198].)

Using a depletion modulator consisting of 3 GaN/AIn QWs inserted in an  $\text{Al}_{0.5}\text{Ga}_{0.5}\text{N}/\text{AlN}$  ridge waveguide on sapphire, Lupu *et al* [197] reported a variation of the refractive index around  $\sim 1.5 \mu\text{m}$  deduced from the shift of the beating interference maxima for different order modes. The change in the refractive index was derived to be  $\Delta n = -5 \times 10^{-3}$  as the population was changed from complete depletion to full population of the QWs. This result is in close agreement with the observation of a refractive index dispersion between  $-5 \times 10^{-3}$  to  $6 \times 10^{-3}$  in a 100-period Si-doped GaN/AIn (1.5 nm/3 nm) MQWs using a free-space Mach–Zehnder interferometer configuration [198]. Figure 11 illustrates the ISB absorption and variation of refractive index measured in such samples. The values of  $\Delta n$  are comparable to those obtained at the same wavelength in phase modulators based on interband transitions in InGaAsP/InP QWs using the quantum confined Stark effect [199], and they are one order of magnitude higher than the index variation obtained in silicon [200]. These results open the way for the realization of ISB Mach–Zehnder interferometer phase modulators in the optical communication wavelength range.

## 6. Infrared photodetectors

### 6.1. Quantum well/quantum dot infrared photodetectors

Quantum well infrared photodetectors (QWIPs) have found widespread application for thermal imaging, using mature materials such as GaAs. In nitrides, however, with the possibility of tuning ISB transitions in the 1.3–1.55  $\mu\text{m}$  range, and with rapid carrier relaxation ( $\sim 140$  fs), the main motivation for QWIPs is high-speed detectors for optical communications. Photoconductive GaN/AlN QWIPs operating at 1.6–1.76  $\mu\text{m}$  have been demonstrated [201, 202]. The responsivity was estimated to be 0.1  $\text{mA W}^{-1}$  at 10 K; however, the photocurrent signal could only be observed up to 120–170 K, even though the optical absorption remained unchanged up to room temperature. Later, Uchida *et al* demonstrated GaN/AlN QWIPs operating at 1.55  $\mu\text{m}$  at room temperature with a responsivity of 0.11  $\text{mA W}^{-1}$  under 15 V bias. Finally, photoconductive IR photodetectors based on cubic GaN/AlN QW superlattices have also been reported [203]. These devices exhibit a photovoltaic effect that is overtaken by the dark current for temperatures above 215 K. This photoresponse is consistent with ISB transition phenomena, but the mechanism behind the photovoltaic behavior remains unknown.

Lateral QDIPs have also been fabricated by depositing planar contacts on samples consisting of 20 periods of Si-doped GaN/AlN QDs, first operating at liquid nitrogen temperature [204] and then at room temperature [127, 205]. The devices exhibit photocurrent for TM-polarized excitation in the 1.4–1.9  $\mu\text{m}$  spectral range, following the intraband  $s$ - $p_z$  selection rules. At low temperature ( $T = 10$  K), mid-IR photoresponse to TE-polarized light is also observed and attributed to  $s$ - $p_{xy}$  transitions. The appearance of photocurrent due to these bound-to-bound transitions is attributed to conductivity via lateral hopping [127]. Further studies have shown that deep levels in the AlN barriers may also contribute to the photocurrent, giving rise to negative photoconductivity effects [206].

In spite of these early demonstrations, photoconductive devices keep presenting a low yield due to the large dark current originating from the high density of dislocations in heteroepitaxial III-nitrides ( $\sim 10^9 \text{ cm}^{-2}$ ), particularly in GaN/AlN devices targeting near-IR wavelengths. An alternative to bypass the leakage problem consists of exploiting the device's photovoltaic response, where zero-bias operation guarantees a minimum dark current. Photoconductive QWIPs already displayed a photovoltaic response [207], which was less sensitive to defects [202], particularly to those associated with the yellow band in GaN [208], in agreement with observations in photovoltaic versus photoconductive interband detectors [209].

The photovoltaic operation of GaN/AlN QWIPs at telecommunication wavelengths and at room temperature was first studied in detail by Hofstetter *et al* [29, 59, 210–212]. The working principle of photovoltaic ISB detectors is based on resonant optical rectification processes in asymmetric QWs [29], as described by Rosencher and Bois in asymmetric GaAs/AlGaAs QWs [213]. In a GaN/AlN superlattice, due

to the QW asymmetric potential profile, the excitation of an electron into the upper quantized level is accompanied by a small displacement in the growth direction, and an electrical dipole moment is created. For a high electron density and many QWs, these microscopic dipole moments add up to a macroscopic polarization of the crystal, which can be detected as an external photovoltage. A strong performance enhancement (responsivity increase by a factor of 60) of these detectors has been achieved by using QDs instead of QWs in the active region [214]. The improvement is attributed to the longer electron lifetime in the upper QD states and the increased lateral electron displacement.

An interesting application of photovoltaic ISB photodetectors is the so-called multi-spectral detectors, operating in various wavelength ranges, with potential applications in surveillance, failure analysis and meteorology. Hofstetter *et al* [215, 216] have combined optical interband and ISB transitions with a monolithic integration of a photoconductive UV interband (solar-blind) detector based on an AlGaIn thin film and a photovoltaic near-IR ISB detector based on an AlN/GaN superlattice, as illustrated in figure 12. The two detectors exhibit spectrally narrow responsivity curves, thus enlarging the UV-to-visible rejection ratio in the case of the UV device, and improving the noise behavior in the case of the IR detector at room temperature.

### 6.2. Quantum cascade detectors

Quantum cascade detectors (QCDs) are photovoltaic devices consisting of several periods of an active QW coupled to a short-period superlattice which serves as an extractor [217, 218]. Under illumination, electrons from the ground state,  $e_1$ , are excited to the upper state of the active QW,  $e_2$ , and then transferred to the extractor region where they experience multiple relaxations toward the next active QW. This results in a macroscopic photovoltage in an open circuit configuration. As major advantage, their dark current is extremely low and the capacitance can be reduced by increasing the number of periods, which enables high frequency response.

GaN/AlGaIn QCDs operating in the near-IR have been reported [219, 220], with their structure illustrated in figure 13. These devices take advantage of the polarization-induced internal electric field to design an efficient AlGaIn/AlN electron extractor where the energy levels are separated by approximately the LO-phonon energy ( $\sim 90$  meV), forming a phonon ladder. The peak responsivity of these GaN/AlGaIn QCDs at room temperature was  $\sim 10 \text{ mA W}^{-1}$  ( $\sim 1000 \text{ V W}^{-1}$ ) [219]. Detectors containing 40 periods of active region with the size  $17 \times 17 \mu\text{m}^2$  exhibit the  $BW_{-3\text{dB}}$  cut-off frequency at 19.7 GHz [221]. However, the speed of these quantum cascade detectors is governed by their  $RC$  constant, and not by an intrinsic mechanism. Pump and probe measurements of these devices pointed to an ISB scattering time in the active QW of 0.1 ps and a transit time through the extractor of 1 ps [222]. With these data, the intrinsic frequency bandwidth is expected to be above 160 GHz, significantly higher than theoretical predictions by Gryshchenko *et al* [223].

Sakr *et al* [224] have shown a significant improvement of a GaN/AlGaIn QCD in terms of responsivity and bandwidth,



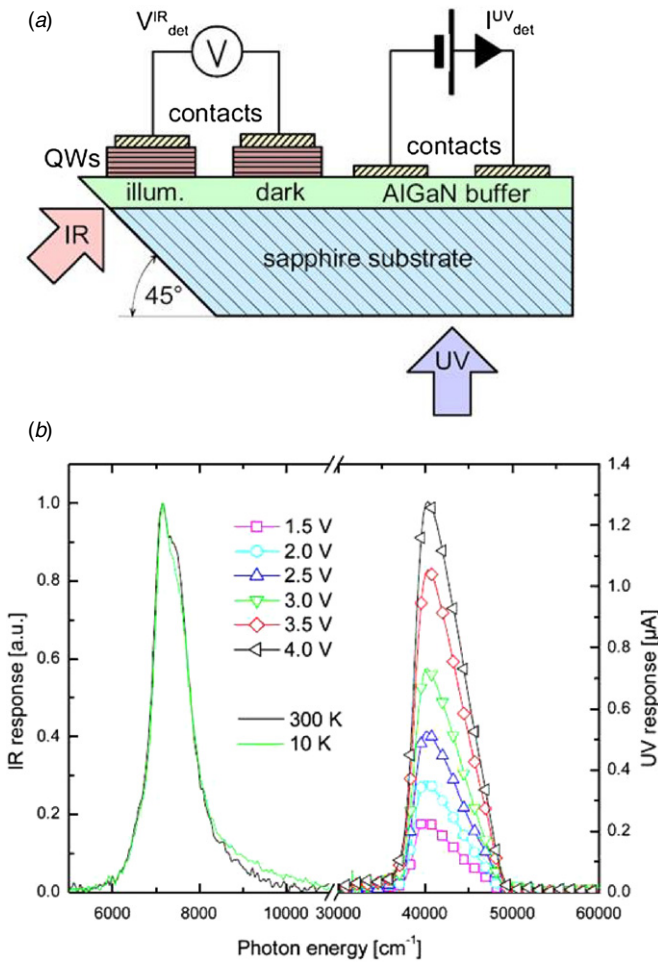


**Figure 12.** (a) Schematic cross section through the sample showing the relative positions of the UV and the IR detector. The QWs are used as the detection layer for the IR, while the AlGaN buffer is the detection layer for the UV radiation. (b) Measured spectral responsivity curves for the UV (1.5 to 4.0 V in steps of 0.5 V at 300 K) and the IR detector (10 and 300 K) (after [216]).

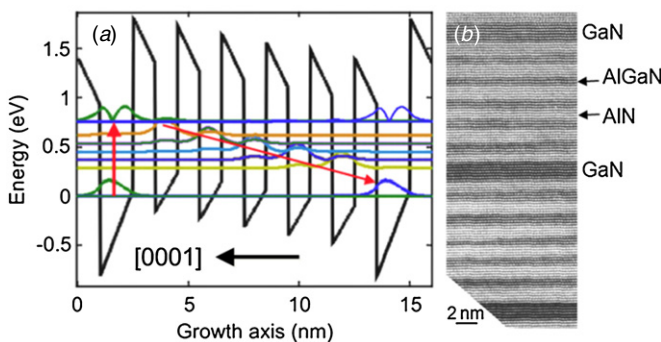


**Figure 13.** (a) Band diagram and energy levels in one stage of the structure. (b) HRTEM image of a period of the structure (active GaN QW followed by five-period AlGaN/AlN extractor), viewed along the  $\langle 11-20 \rangle$  axis. Reprinted with permission from [219]. Copyright 2008, American Institute of Physics.

reaching at least  $9.5 \pm 2 \text{ mA W}^{-1}$  for  $10 \times 10 \mu\text{m}^2$  devices at  $1.5 \mu\text{m}$  peak detection wavelength at room temperature, with a  $BW_{-3\text{dB}}$  frequency response of  $\sim 40 \text{ GHz}$ . The enhanced responsivity is achieved by illuminating the side facet of the

QCDs (illumination perpendicular to the growth axis), as a result of the good coupling between TM-polarized waveguide-propagated light and ISB transitions. The frequency bandwidth is improved by reducing the top contact resistance and the contact layer resistivity, as well as the device capacitance through increasing the number of periods.

Based on the presence of the internal field in III-nitride QWs, symmetry breaking of the potential permits ISB transitions not only between the ground electronic state and the first excited state,  $e_1 \rightarrow e_2$ , but also between  $e_1$  and the second excited state,  $e_3$ , a transition forbidden in symmetric QWs [14]. This feature was exploited for the fabrication of a two-color GaN-based QCD operating at  $1.7$  and  $1 \mu\text{m}$  at room temperature absorption wavelengths associated to the  $e_1 \rightarrow e_2$  and  $e_2 \rightarrow e_3$  transitions, respectively [225]. It should be noted that although the oscillator strength associated with  $e_1 \rightarrow e_3$  is 21 times smaller than that of  $e_1 \rightarrow e_2$ , the responsivity at  $1 \mu\text{m}$  is only 12 times smaller than that at  $1.7 \mu\text{m}$ . This is a consequence of the increased transfer efficiency into the extractor for electrons in the  $e_3$  subband due to the lower effective barrier and of the multiple relaxation paths to the extractor stage.

Finally, a simplified QCD design where the extractor superlattice has been replaced by an AlGaN layer has been proposed [226]. The thickness and composition of the extractor alloy is chosen so that the energy separation between the ground state of the extractor and the ground state of the active QW is close to the LO-phonon energy. An alloy-extractor device presenting peak photovoltaic response at  $1.9 \mu\text{m}$  has been demonstrated [226].

### 6.3. THz intersubband photodetectors

The first demonstration of a nitride-based THz ISB photodetector has been reported by Sudradjat *et al* [227]. In the far-IR spectral region, a reduction of the dislocation density allows for the fabrication of photoconductive QWIPs. A key design element for these devices is the optimization between two conflicting requirements: (i) the need for large oscillator strength of the absorbing transitions, which is favored by the use of well-confined upper subbands, and (ii) the efficient escape of the photoexcited electron out of the QW, which is favored by absorbing from a bound level directly into the continuum. A good compromise is attained with QWs whose first excited state is nearly resonant with the conduction band edge in the barriers, leading to what are commonly referred to as *bound-to-quasi-bound absorbing transitions* [10]. This was achieved in nitride-based THz ISB photodetectors by creating a nearly flat potential profile using the step-QW design [91], so that the first excited subband can be positioned at any desired energy relative to the top of the barriers by changing the QW thickness (see figure 14(a)), imitating the design of As-based structures. The fabricated devices present a photocurrent spectrum centered at  $23 \mu\text{m}$  wavelength ( $=13 \text{ THz}$  frequency), well resolved from low temperature ( $T = 20 \text{ K}$  in figure 14(b)) up to  $T = 50 \text{ K}$ , with a responsivity of approximately  $7 \text{ mA W}^{-1}$  [227].



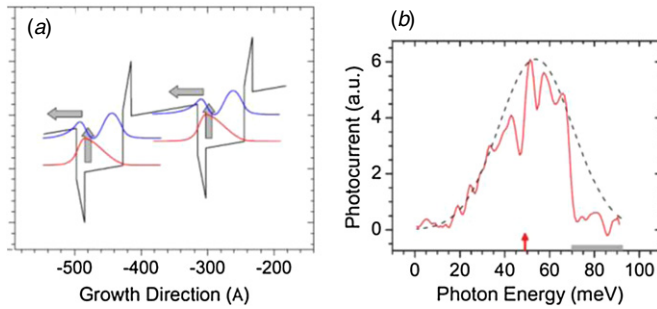


**Figure 14.** (a) Conduction band profile of an AlGaIn far-IR QWIP structure under bias, where each repeat unit consists of an  $\text{Al}_{0.16}\text{Ga}_{0.84}\text{N}$  barrier and a  $\text{GaN}/\text{Al}_{0.08}\text{Ga}_{0.92}\text{N}$  step-QW. The squared envelope functions of the ground-state and first excited state of each QW are also shown, referenced to their respective energy levels. The vertical and horizontal arrows indicate, respectively, photon absorption and photoelectron escape into the continuum of unbound states over the barriers. (b) Photocurrent spectrum of a double-step-QW AlGaIn THz QWIP measured at  $T = 20$  K under 0.8 V bias (solid line), and Gaussian fit (dashed line). The grey band near the horizontal axis indicates the Reststrahlen band of GaN. The vertical arrow marks the calculated transition energy. Reprinted with permission from [227]. Copyright 2012, American Institute of Physics.

## 7. Toward the quantum cascade laser

### 7.1. Light emission in superlattices

ISB luminescence is an inefficient process due to competition with nonradiative electron relaxation via interactions with LO phonons (sub-picosecond), or electron–electron interactions and impurity scattering (tens of picoseconds). However, this does not hinder the realization of QCLs: in the population inversion regime, short radiative lifetime and high stimulated gain can be achieved thanks to the strong ISB transitional oscillator strength.

Despite of the inefficiency of the process, room-temperature ISB luminescence in the  $2\text{--}2.3\ \mu\text{m}$  spectral range has been observed in  $\text{GaN}/\text{AlN}$  MQWs under optical pumping [228–230]. The QWs were designed to exhibit three bound states in the conduction band. The emission arises from the  $e_3\text{--}e_2$  ISB transition. Photoluminescence excitation spectroscopy shows that the emission is only observed for TM-polarized excitation at wavelengths corresponding to the  $e_1\text{--}e_3$  ISB transition.

Room-temperature intraband emission has also been observed in optically pumped  $\text{GaN}/\text{AlN}$  quantum dots [231]. The  $p_z$ -s intraband luminescence was observed at  $\lambda = 1.48\ \mu\text{m}$  under optical excitation at  $\lambda = 1.34\ \mu\text{m}$  perpendicular to the  $[0001]$  growth axis. The population of the  $p_z$  state arises from Raman scattering by  $\text{GaN}$   $A_1$  longitudinal optical phonons. Based on the emission spectral shape, we estimate that the homogeneous linewidth of the  $s\text{--}p_z$  intraband transition is less than 4 meV.

In spite of these observations, further work is required in terms of growth optimization, processing and dedicated laser active region and cavity design in order to develop quantum fountain lasers.

### 7.2. Quantum cascade laser structures

QCLs rely on transitions between quantized conduction band states of a suitably designed semiconductor MQW structure [11]. Due to the polarization selection rules associated with ISB transitions, these devices are in-plane emitters, with their electric-field vector perpendicular to the plane of the layers. An electron injected into the *active QWs* first undergoes an ISB lasing transition, and is rapidly extracted by a fast non-radiative transition, which maintains the population inversion. Then, the electron tunnels through the *injector region* toward the upper level of the next active QWs. By using several tens or even hundreds of periods of active region + injector in a series (a cascade), higher optical gains and multiple photons per electron are obtained. The emitting wavelength can be tuned in the range of a few microns to well above  $10\ \mu\text{m}$ , by changing the design parameters, such as the quantum well (QW) thickness and barrier height.

Typical QCLs have been engineered and fabricated using arsenide-based systems such as  $\text{AlGaAs}$  and  $\text{InGaAs}$  and  $\text{AlInAs}/\text{GaInAs}/\text{InP}$ . These complex GaAs-based structures require precise structure control and excellent homogeneity of the material, both in plane and along the multiple periods that compose the active region. Due to the large lattice mismatch and defect structure of the  $\text{GaN}/\text{AlN}$  system, the fabrication of GaN-based QCLs operating in the near-IR does not appear feasible, despite several theoretical proposals [16, 232, 233] and promising results in terms of waveguide fabrication [234]. However, there is an increasing interest and research effort for the fabrication of the first GaN QCL in the far-IR, particularly in the so-called THz domain, spectral region where the lattice mismatch of the structure is reduced, and where it should be possible to exploit the large LO phonon of III-nitrides in order to realize devices operating at room temperature.

Since the first demonstration of a THz QCL in 2001 [235] rapid progress has been made in terms of device performance. To date, QCL has been demonstrated in the  $0.85\text{--}5$  THz range [236], with pulsed operation up to 186 K [237, 238], and pulsed output powers of up to 250 mW [239]. The devices have evolved through different designs including the resonant-phonon, the chirped superlattice, bound-to-continuum and hybrid designs [237, 240]. There are two major processes that cause the degradation of population inversion (and thus gain) in THz QCLs at high temperature: thermal backfilling and thermally activated phonon scattering. Backfilling of the lower radiative state with electrons from the heavily populated injector occurs either by thermal excitation (according to the Boltzmann distribution), or by reabsorption of non-equilibrium LO-phonons (the hot-phonon effect) [241]. The other main degradation mechanism is the onset of thermally activated LO-phonon scattering, as electrons in the upper radiative state acquire sufficient in-plane kinetic energy to emit an LO-phonon and relax nonradiatively to the lower radiative state. This causes the upper-state lifetime  $\tau_{21}$  to decrease exponentially according to

$$\tau_{12} \propto \exp[-(E_{\text{LO}} - h\nu)/k_{\text{B}}T_e], \quad (15)$$

where  $h\nu$  is the THz photon energy, and  $k_{\text{B}}$  is the Boltzmann constant. Both of these mechanisms greatly depend on the

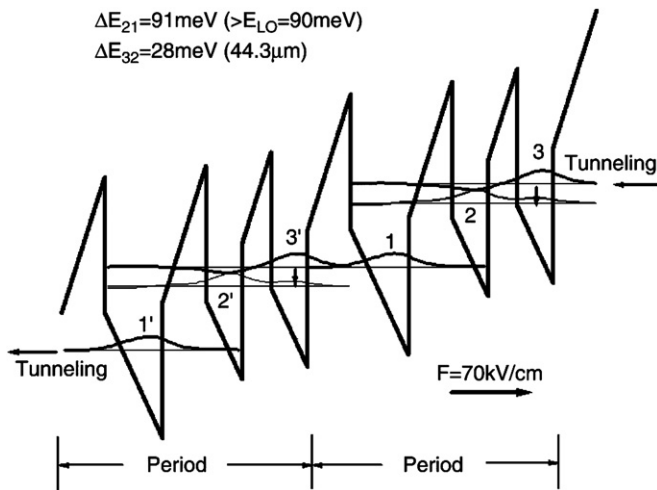


**Figure 15.** Band structure, subband energy separations and envelope wave functions of the active region of the proposed AlGaIn THz QCL structure. Two periods are shown, each with 3 QWs with layer thicknesses as (nm): 3, 4, 3, 2.5, 2 and 2.5. Wells underlined and barriers plain. The transition from 3–2 is engineered through a coupled QW to be 28 meV, while the 2–1 transition is engineering to be on the order of the longitudinal optical phonon (90 meV). With an applied bias of  $70 \text{ kV cm}^{-1}$ , tunneling between states 1 and 3 occurs in for the cascade effect and carrier recycling. Reprinted from [243], with permission from Elsevier.

electron gas temperature  $T_e$ , which is 50–100 K higher than the lattice temperature during device operation.

In general, resonant-phonon QCL designs show the best temperature performance. In this scheme, injector states are designed so that the lower radiative state is resonantly coupled into the upper injector level, which is separated by approximately the LO-phonon energy from the second injector level, providing efficient depopulation of the lower lasing state and a fast relaxation path toward the upper radiative state. The explicit inclusion of an LO-phonon scattering event for depopulation means that resonant-phonon designs present a relatively large energetic barrier (about one LO phonon) to thermal backfilling. However, the low LO-phonon energy in arsenide compounds constitutes a major bottleneck for operation at higher temperatures. Furthermore, the LO phonon of GaAs systems causes an unobtainable emission gap in lasing systems (Reststrahlen band at 8–9 THz), which is an intrinsic property of the material system.

Nitride semiconductors, namely GaN, have an LO phonon energy of 92 meV, much higher than the ambient thermal energy. A number of designs for a GaN THz QCL have been proposed [214, 242–249], all focusing on the resonant-phonon architecture first theorized in 2003 [240]. Figure 15 presents the basic device structure for polar III-nitrides. Below we summarize the efforts of various groups working on this topic, who have introduced design improvements but keep the same underlying concept.

Researchers from the University of Leeds (UK) have engineered one of the first designs for GaN-based QCLs using a fully consistent scattering rate equation model [242], and an energy balance method [250]. Both electron–LO-phonon and electron–electron scattering mechanisms are taken

into account. They have created a contour plot outlining the wavelengths of emission theorized with different well and barrier thickness within a superlattice, after appropriate strain balancing [232]. They have also proposed a  $34 \mu\text{m}$  wavelength QCL design in both the  $a$  and  $c$  planes [242]. Population inversions in active laser states up to 19% for the  $a$ -plane, and up to 40% for the  $c$ -plane design, are predicted and, based on estimated modal gain and waveguide/mirror losses, they conclude that the observation of laser action in GaN/AlGaIn cascades should be feasible in both planes.

Terashima and Hirayama (RIKEN, Japan) have presented THz QCL designs based on four-well resonant-phonon GaN/AlGaIn structures [246, 251, 252]. The structures have been synthesized by PAMBE using a ‘droplet elimination by thermal annealing’ technique [51], and they have been processed in a single-metal plasmon waveguide geometry [246, 252]. Electronluminescence at 1.37 THz has been reported in a first structure [251], and polarization-dependent electroluminescence at 2.82 THz, slightly tunable by changing the driving voltage in the 20–21 V range, has been reported using a second design [252].

The group of Paiella and Moustakas at Boston University has proposed a QCL design emitting at 2 THz, designed using a Schrödinger-equation solver based on the effective-mass approximation, with the characteristic built-in electric fields of nitride heterostructures included explicitly [245]. They have also performed a rigorous comparison between a GaAs/AlGaAs and the GaN/AlGaIn THz QCLs emitting at the same wavelength using a microscopic model of carrier dynamics in QCL gain media based on a set of Boltzmann-like equations solved with a Monte Carlo technique [245, 253]. Results show that the population inversion within GaN lasers is much less dependent on temperature than conventional GaAs designs, as presented in figure 16. From the experimental viewpoint, they have explored tunneling effects in cascade-like superlattices, their temperature dependence and the effect of bias for multiple device architectures [254].

Mirzaei *et al* have proposed a dual-wavelength QCL to emit at both 33 and  $52 \mu\text{m}$  with similar behavior of the output optical power for both wavelengths [249]. The design uses the LO-phonon resonance to extract electrons from the lower radiative levels, and incorporates a miniband injector, theorized via rate equation analysis to operate properly up to 265 K.

Chou *et al* have modeled GaN-based resonant-phonon THz lasers using a transfer matrix method, paying particular attention to the effect of the strain state [248]. They predict higher THz power in GaN/AlGaIn heterostructures as compared to heterostructures incorporating In [255].

Finally, Yasuda *et al* have used the non-equilibrium Green’s function to model GaN THz QCL devices, namely a four-well resonant-phonon InAlGaIn/GaN structure on (0001)-oriented GaN [247], and a two-well non-polar GaN/AlGaIn structure [256].

Overall, many different designs from various simulation models have been presented. They all focus on the resonant-phonon architecture and predict functionality at high temperatures. Some devices have been fabricated, but

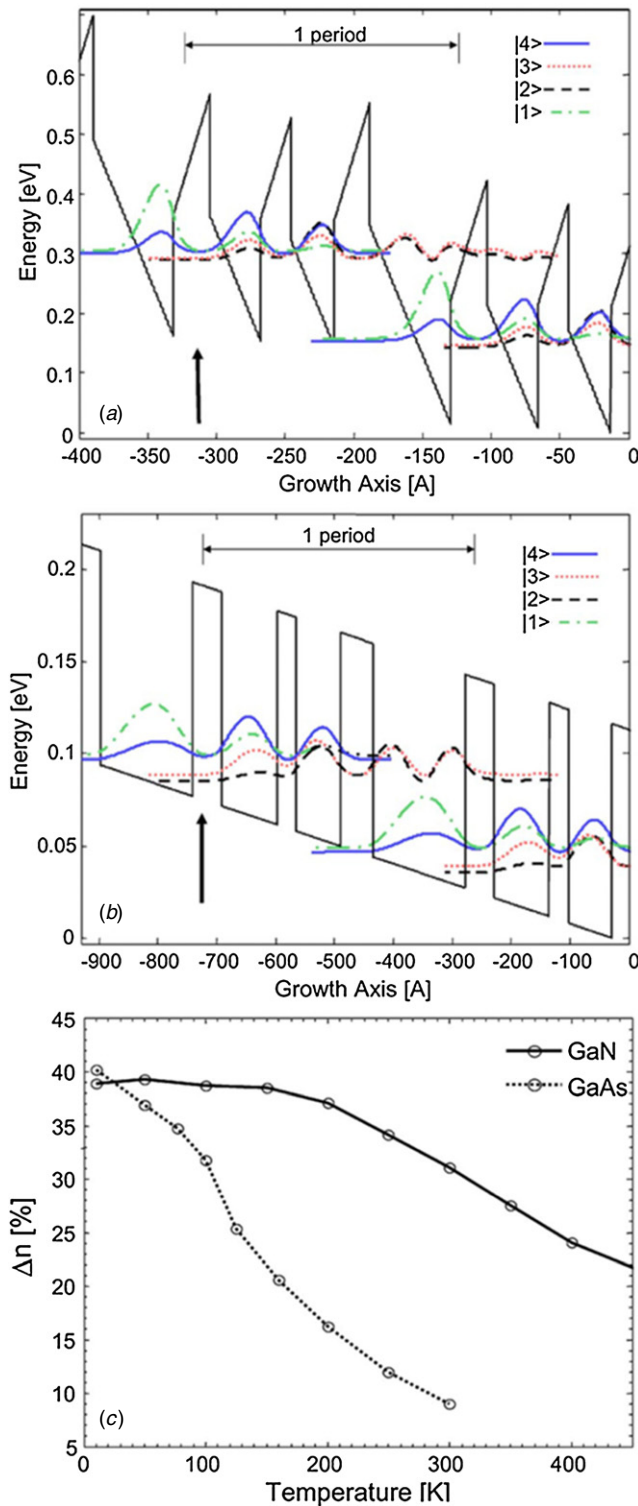


**Figure 16.** Conduction-band profile and squared envelope functions of (a) a GaN/Al<sub>0.15</sub>Ga<sub>0.85</sub>N and (b) a GaAs/Al<sub>0.15</sub>Ga<sub>0.85</sub>As QCL gain media both for emission at 2 THz. The two structures are plotted in the presence of an external field of (a) 73 kV cm<sup>-1</sup> and (b) 11 kV cm<sup>-1</sup>. The layer thicknesses of a single stage, starting from the injection barrier (indicated by the arrow) and moving downstream, are **26/37/22/31/26/59** Å for the GaN structure and **49/94/33/74/56/156** Å for the GaAs structure (the boldfaced numbers refer to the barrier layers). (c) Calculated fractional population inversion of the THz QCL structures in (a), indicated by the solid line, and (b), indicated by the dotted line. Reprinted with permission from [245]. Copyright 2008, American Institute of Physics.

none have shown lasing properties. All the current research suggests that THz QCL devices are feasible, but there are still numerous problems for device engineering including the unavailability of substrates, difficult band engineering, weak current transport as well as the problems from lattice mismatch [232], doping [234] and waveguide construction [233]. The above-summarized papers have provided solutions toward managing the optical/electronic design, the lattice mismatch and fabrication methodology, but the fabrication of a functioning laser device remains a challenge.

## 8. Conclusions and perspectives

In this paper, we have reviewed recent research on III-nitride ISB optoelectronics. III-nitride heterostructures are excellent candidates for high-speed ISB devices in the near-IR thanks to their large conduction band offset (~1.8 eV for the GaN/AlN system) and subpicosecond ISB scattering rates. However, bandgap engineering requires exquisite control of material growth and modeling that are notoriously difficult in GaN/AlGaIn. First prototypes of nitride-based ISB devices are room-temperature multi-Tbit/s all-optical switches operating at 1.5 μm, photovoltaic and photoconductive QWIPs, QDIPs and ISB electro-optical modulators. Near-IR ISB luminescence from GaN/AlN QWs and QDs has been reported. The concept of quantum cascade applied to III-nitrides has been demonstrated by the development of QCDs operating in the 1.0–4.5 μm spectral range.

An emerging field for GaN-based ISB devices is the extension toward the far-IR spectral range, with several theoretical designs of GaN QCLs recently reported. At far-IR wavelengths, the large GaN LO-phonon energy (92 meV) becomes a valuable property to achieve ISB operation at relatively high temperatures, and also to cover IR wavelengths that are not accessible by other III–V semiconductors due to Reststrahlen absorption. However, the extension of this ISB technology toward longer wavelengths requires a reduction of the polarization-induced internal electric field, which sets new material challenges.

## Acknowledgment

This work is supported by the EU ERC-StG ‘TeraGaN’ (#278428) project.

## References

- [1] Kamgar A, Kneschaurek P, Dorda G and Koch J 1974 Resonance spectroscopy of electronic levels in a surface accumulation layer *Phys. Rev. Lett.* **32** 1251–4
- [2] Ando T, Fowler A B and Stern F 1982 Electronic properties of two-dimensional systems *Rev. Mod. Phys.* **54** 437–672
- [3] Esaki L and Sakaki H 1977 New photoconductor *IBM Tech. Discl. Bull.* **20** 2456–7
- [4] Chiu L C, Smith J S, Margalit S, Yariv A and Cho A Y 1983 Application of internal photoemission from quantum-well and heterojunction superlattices to infrared photodetectors *Infrared Phys.* **23** 93–7



- [5] Smith J S, Chiu L C, Margalit S, Yariv A and Cho A Y 1983 A new infrared detector using electron emission from multiple quantum wells *J. Vac. Sci. Technol. B* **1** 376–8
- [6] Coon D D and Karunasiri R P G 1984 New mode of IR detection using quantum wells *Appl. Phys. Lett.* **45** 649–51
- [7] Coon D D, Karunasiri R P G and Liu H C 1986 Fast response quantum well photodetectors *J. Appl. Phys.* **60** 2636–8
- [8] West L C and Eglash S J 1985 First observation of an extremely large-dipole infrared transition within the conduction band of a GaAs quantum well *Appl. Phys. Lett.* **46** 1156–8
- [9] Levine B F, Choi K K, Bethea C G, Walker J and Malik R J 1987 New 10  $\mu\text{m}$  infrared detector using intersubband absorption in resonant tunneling GaAlAs superlattices *Appl. Phys. Lett.* **50** 1092–4
- [10] Levine B F 1993 Quantum-well infrared photodetectors *J. Appl. Phys.* **74** R1–81
- [11] Faist J, Capasso F, Sivco D L, Sirtori C, Hutchinson A L and Cho A Y 1994 Quantum cascade laser *Science* **264** 553–6
- [12] Binggeli N, Ferrara P and Baldereschi A 2001 Band-offset trends in nitride heterojunctions *Phys. Rev. B* **63** 245306
- [13] Cociorva D, Aulbur W G and Wilkins J W 2002 Quasiparticle calculations of band offsets at AlN–GaN interfaces *Solid State Commun.* **124** 63–66
- [14] Tchernycheva M, Nevou L, Doyennette L, Julien F, Warde E, Guillot F, Monroy E, Bellet-Amalric E, Remmele T and Albrecht M 2006 Systematic experimental and theoretical investigation of intersubband absorption in GaN/AlN quantum wells *Phys. Rev. B* **73** 125347
- [15] Suzuki N and Iizuka N 1997 Feasibility study on ultrafast nonlinear optical properties of 1.55- $\mu\text{m}$  intersubband transition in AlGaIn/GaN quantum wells *Japan. J. Appl. Phys.* **36** L1006–8
- [16] Hofstetter D *et al* 2010 Intersubband transition-based processes and devices in AlN/GaN-based heterostructures *Proc. IEEE* **98** 1234–48
- [17] Machhadani H *et al* 2009 GaN/AlGaIn intersubband optoelectronic devices *New J. Phys.* **11** 125023
- [18] Hao M, Mahanty S, Qhalid Fareed R S, Tottori S, Nishino K and Sakai S 1999 Infrared properties of bulk GaN *Appl. Phys. Lett.* **74** 2788–90
- [19] Yang J, Brown G J, Dutta M and Strosio M A 2005 Photon absorption in the reststrahlen band of thin films of GaN and AlN: Two phonon effects *J. Appl. Phys.* **98** 043517
- [20] Welna M, Kudrawiec R, Motyka M, Kucharski R, Zajac M, Rudziński M, Misiewicz J, Doradziński R and Dwiliński R 2012 Transparency of GaN substrates in the mid-infrared spectral range *Cryst. Res. Technol.* **47** 347–50
- [21] Kandaswamy P K, Machhadani H, Bougerol C, Sakr S, Tchernycheva M, Julien F H and Monroy E 2009 Midinfrared intersubband absorption in GaN/AlGaIn superlattices on Si(1 1 1) templates *Appl. Phys. Lett.* **95** 141911
- [22] Kandaswamy P K, Machhadani H, Kotsar Y, Sakr S, Das A, Tchernycheva M, Rapenne L, Sarigiannidou E, Julien F H and Monroy E 2010 Effect of doping on the mid-infrared intersubband absorption in GaN/AlGaIn superlattices grown on Si(1 1 1) templates *Appl. Phys. Lett.* **96** 141903
- [23] Suzuki N and Iizuka N 1998 Electron scattering rates in AlGaIn/GaN quantum wells for 1.55- $\mu\text{m}$  inter-subband transition *Japan. J. Appl. Phys.* **37** L369–71
- [24] Bastard G 1988 *Les Editions de Physique Wave mechanics applied to semiconductor heterostructures* (Les Ulis Cedex: Halsted Press)
- [25] Liu H C and Capasso F 2000 *Physics and Device Applications I Intersubband transitions in quantum wells* (San Diego, CA: Academic)
- [26] Bernardini F, Fiorentini V and Vanderbilt D 1997 Spontaneous polarization and piezoelectric constants of III–V nitrides *Phys. Rev. B* **56** R10024–7
- [27] Birner S, Zibold T, Andlauer T, Kubis T, Sabathil M, Trellakis A and Vogl P 2007 Nextnano: general purpose 3D simulations *IEEE Trans. Electron Devices* **54** 2137–42
- [28] Kandaswamy P K *et al* 2008 GaN/AlN short-period superlattices for intersubband optoelectronics: a systematic study of their epitaxial growth, design, and performance *J. Appl. Phys.* **104** 093501
- [29] Hofstetter D, Baumann E, Giorgetta F R, Guillot F, Leconte S and Monroy E 2007 Optically nonlinear effects in intersubband transitions of GaN/AlN-based superlattice structures *Appl. Phys. Lett.* **91** 131115
- [30] Nevou L, Tchernycheva M, Julien F, Raybaut M, Godard A, Rosencher E, Guillot F and Monroy E 2006 Intersubband resonant enhancement of second-harmonic generation in GaN/AlN quantum wells *Appl. Phys. Lett.* **89** 151101
- [31] Nevou L, Mangeney J, Tchernycheva M, Julien F H, Guillot F and Monroy E 2009 Ultrafast relaxation and optical saturation of intraband absorption of GaN/AlN quantum dots *Appl. Phys. Lett.* **94** 132104
- [32] Sarigiannidou E, Monroy E, Gogneau N, Radtke G, Bayle-Guillemaud P, Bellet-Amalric E, Daudin B and Rouvière J L 2006 Comparison of the structural quality in Ga-face and N-face polarity GaN/AlN multiple-quantum-well structures *Semicond. Sci. Technol.* **21** 612–8
- [33] Gmachl C, Ng H M, George Chu S-N and Cho A Y 2000 Intersubband absorption at  $\lambda \sim 1.55 \mu\text{m}$  in well- and modulation-doped GaN/AlGaIn multiple quantum wells with superlattice barriers *Appl. Phys. Lett.* **77** 3722–4
- [34] Gmachl C, Ng H M and Cho A Y 2001 Intersubband absorption in degenerately doped GaN/Al<sub>0.3</sub>Ga<sub>0.7</sub>N coupled double quantum wells *Appl. Phys. Lett.* **79** 1590–2
- [35] Kishino K, Kikuchi A, Kanazawa H and Tachibana T 2002 Intersubband transition in (GaN)<sub>m</sub>/(AlN)<sub>n</sub> superlattices in the wavelength range from 1.08 to 1.61  $\mu\text{m}$  *Appl. Phys. Lett.* **81** 1234–6
- [36] Iizuka N, Kaneko K and Suzuki N 2002 Near-infrared intersubband absorption in GaN/AlN quantum wells grown by molecular beam epitaxy *Appl. Phys. Lett.* **81** 1803–5
- [37] Heber J D, Gmachl C, Ng H M and Cho A Y 2002 Comparative study of ultrafast intersubband electron scattering times at  $\sim 1.55 \mu\text{m}$  wavelength in GaN/AlGaIn heterostructures *Appl. Phys. Lett.* **81** 1237–9
- [38] Helman A *et al* 2003 Intersubband spectroscopy of doped and undoped GaN/AlN quantum wells grown by molecular-beam epitaxy *Appl. Phys. Lett.* **83** 5196–8
- [39] Zhou Q, Chen J, Pattada B, Manasreh M O, Xiu F, Puntigan S, He L, Ramaiah K S and Morkoç H 2003 Infrared optical absorbance of intersubband transitions in GaN/AlGaIn multiple quantum well structures *J. Appl. Phys.* **93** 10140–2
- [40] Adelmann C, Brault J, Mula G, Daudin B, Lymperakis L and Neugebauer J 2003 Gallium adsorption on (0 0 0 1) GaN surfaces *Phys. Rev. B* **67** 165419
- [41] Neugebauer J, Zywiets T, Scheffler M, Northrup J, Chen H and Feenstra R 2003 Adatom kinetics on and below the surface: the existence of a new diffusion channel *Phys. Rev. Lett.* **90** 056101
- [42] Heying B, Averbek R, Chen L F, Haus E, Riechert H and Speck J S 2000 Control of GaN surface morphologies using plasma-assisted molecular beam epitaxy *J. Appl. Phys.* **88** 1855–60
- [43] Iliopoulos E and Moustakas T D 2002 Growth kinetics of AlGaIn films by plasma-assisted molecular-beam epitaxy *Appl. Phys. Lett.* **81** 295–7



- [44] Monroy E, Daudin B, Bellet-Amalric E, Gogneau N, Jalabert D, Enjalbert F, Brault J, Barjon J and Dang L S 2003 Surfactant effect of In for AlGaIn growth by plasma-assisted molecular beam epitaxy *J. Appl. Phys.* **93** 1550–6
- [45] Koblmüller G, Averbek R, Geelhaar L, Riechert H, Höslér W and Pongratz P 2003 Growth diagram and morphologies of AlN thin films grown by molecular beam epitaxy *J. Appl. Phys.* **93** 9591–7
- [46] Mula G, Adelmann C, Moehl S, Oullier J and Daudin B 2001 Surfactant effect of gallium during molecular-beam epitaxy of GaN on AlN (0001) *Phys. Rev. B* **64** 195406
- [47] Brown J S, Koblmüller G, Wu F, Averbek R, Riechert H and Speck J S 2006 Ga adsorbate on (0001) GaN: *In situ* characterization with quadrupole mass spectrometry and reflection high-energy electron diffraction *J. Appl. Phys.* **99** 074902
- [48] Northrup J, Neugebauer J, Feenstra R and Smith A 2000 Structure of GaN(0001): the laterally contracted Ga bilayer model *Phys. Rev. B* **61** 9932–5
- [49] Koblmüller G, Brown J, Averbek R, Riechert H, Pongratz P and Speck J S 2005 Continuous evolution of Ga adlayer coverages during plasma-assisted molecular-beam epitaxy of (0001) GaN *Appl. Phys. Lett.* **86** 041908
- [50] Moseley M, Billingsley D, Henderson W, Trybus E and Doolittle W A 2009 Transient atomic behavior and surface kinetics of GaN *J. Appl. Phys.* **106** 014905
- [51] Terashima W and Hirayama H 2010 The utility of droplet elimination by thermal annealing technique for fabrication of GaN/AlGaIn terahertz quantum cascade structure by radio frequency molecular beam epitaxy *Appl. Phys. Express* **3** 125501
- [52] Koblmüller G, Reurings F, Tuomisto F and Speck J S 2010 Influence of Ga/N ratio on morphology, vacancies, and electrical transport in GaN grown by molecular beam epitaxy at high temperature *Appl. Phys. Lett.* **97** 191915
- [53] Gogneau N, Jalabert D, Monroy E, Sarigiannidou E, Rouvière J L, Shibata T, Tanaka M, Gerard J M and Daudin B 2004 Influence of AlN overgrowth on structural properties of GaN quantum wells and quantum dots grown by plasma-assisted molecular beam epitaxy *J. Appl. Phys.* **96** 1104–10
- [54] Grandjean N and Massies J 1996 Kinetics of surfactant-mediated epitaxy of III–V semiconductors *Phys. Rev. B* **53** R13231–4
- [55] Widmann F, Daudin B, Feuillet G, Pelekanos N and Rouvière J L 1998 Improved quality GaN grown by molecular beam epitaxy using In as a surfactant *Appl. Phys. Lett.* **73** 2642–4
- [56] Kruse C, Einfeldt S, Böttcher T and Hommel D 2001 In as a surfactant for the growth of GaN (0001) by plasma-assisted molecular-beam epitaxy *Appl. Phys. Lett.* **79** 3425–7
- [57] Monroy E, Guillot F, Gayral B, Bellet-Amalric E, Jalabert D, Gérard J-M, Si Dang L, Tchernycheva M and Julien F H 2006 Observation of hot luminescence and slow inter-sub-band relaxation in Si-doped GaN/Al<sub>x</sub>Ga<sub>1-x</sub>N ( $x = 0.11, 0.25$ ) multi-quantum-well structures *J. Appl. Phys.* **99** 093513
- [58] Kandaswamy P K, Bougerol C, Jalabert D, Ruterana P and Monroy E 2009 Strain relaxation in short-period polar GaN/AlN superlattices *J. Appl. Phys.* **106** 013526
- [59] Baumann E *et al* 2006 Near infrared absorption and room temperature photovoltaic response in AlN/GaN superlattices grown by metal-organic vapor-phase epitaxy *Appl. Phys. Lett.* **89** 041106
- [60] Bayram C, Péré-laperne N and Razeghi M 2009 Effects of well width and growth temperature on optical and structural characteristics of AlN/GaN superlattices grown by metal-organic chemical vapor deposition *Appl. Phys. Lett.* **95** 201906
- [61] Sodabanlu H, Yang J-S, Sugiyama M, Shimogaki Y and Nakano Y 2009 Strain effects on the intersubband transitions in GaN/AlN multiple quantum wells grown by low-temperature metal organic vapor phase epitaxy with AlGaIn interlayer *Appl. Phys. Lett.* **95** 161908
- [62] Yang J-S, Sodabanlu H, Sugiyama M, Nakano Y and Shimogaki Y 2009 Blueshift of intersubband transition wavelength in AlN/GaN multiple quantum wells by low temperature metal organic vapor phase epitaxy using pulse injection method *Appl. Phys. Lett.* **95** 162111
- [63] Nicolay S, Feltin E, Carlin J-F, Grandjean N, Nevou L, Julien F H, Schmidbauer M, Remmele T and Albrecht M 2007 Strain-induced interface instability in GaN/AlN multiple quantum wells *Appl. Phys. Lett.* **91** 061927
- [64] Iizuka N, Kaneko K and Suzuki N 2006 All-optical switch utilizing intersubband transition in GaN quantum wells *IEEE J. Quantum Electron.* **42** 765–71
- [65] Floro J A, Follstaedt D M, Provencio P, Hearne S J and Lee S R 2004 Misfit dislocation formation in the AlGaIn/GaN heterointerface *J. Appl. Phys.* **96** 7087–94
- [66] Matthews J W and Blakeslee A E 1974 Defects in epitaxial multilayers *J. Cryst. Growth* **27** 118–25
- [67] Ponce F A 1997 Defects and interfaces in GaN epitaxy *MRS Bull.* **22** 51–57
- [68] Moran B, Wu F, Romanov A E, Mishra U K, Denbaars S P and Speck J S 2004 Structural and morphological evolution of GaN grown by metalorganic chemical vapor deposition on SiC substrates using an AlN initial layer *J. Cryst. Growth* **273** 38–47
- [69] Kehagias T, Delimitis A, Komninou P, Iliopoulos E, Dimakis E, Georgakilas A and Nouet G 2005 Misfit accommodation of compact and columnar InN epilayers grown on Ga-face GaN (0001) by molecular-beam epitaxy *Appl. Phys. Lett.* **86** 151905
- [70] Hearne S J, Han J, Lee S R, Floro J A, Follstaedt D M, Chason E and Tsong I S T 2000 Brittle-ductile relaxation kinetics of strained AlGaIn/GaN heterostructures *Appl. Phys. Lett.* **76** 1534–6
- [71] Liu R, Mei J, Srinivasan S, Ponce F A, Omiya H, Narukawa Y and Mukai T 2006 Generation of misfit dislocations by basal-plane slip in InGaIn/GaN heterostructures *Appl. Phys. Lett.* **89** 201911
- [72] Einfeldt S, Heinke H, Kirchner V and Hommel D 2001 Strain relaxation in AlGaIn/GaN superlattices grown on GaN *J. Appl. Phys.* **89** 2160–7
- [73] Andersson T G, Liu X Y, Aggerstam T, Holmström P, Lourduos S, Thylen L, Chen Y L, Hsieh C H and Lo I 2009 Macroscopic defects in GaN/AlN multiple quantum well structures grown by MBE on GaN templates *Microelectron. J.* **40** 360–2
- [74] Cherns P D, McAleese C, Kappers M J and Humphreys C J 2007 Microscopy of Semiconducting Materials *Strain relaxation in an AlGaIn/GaN quantum well system* ed A G Cullis and P A Midgley (Dordrecht: Springer) pp 25–28
- [75] Cantu P, Wu F, Waltereit P, Keller S, Romanov A E, DenBaars S P and Speck J S 2005 Role of inclined threading dislocations in stress relaxation in mismatched layers *J. Appl. Phys.* **97** 103534
- [76] Bellet-Amalric E, Adelmann C, Sarigiannidou E, Rouvière J L, Feuillet G, Monroy E and Daudin B 2004 Plastic strain relaxation of nitride heterostructures *J. Appl. Phys.* **95** 1127–33
- [77] Kotsar Y, Doisneau B, Bellet-Amalric E, Das A, Sarigiannidou E and Monroy E 2011 Strain relaxation in GaN/Al<sub>x</sub>Ga<sub>1-x</sub>N superlattices grown by plasma-assisted molecular-beam epitaxy *J. Appl. Phys.* **110** 033501

- [78] Yang R, Xu J and Sweeny M 1994 Selection rules of intersubband transitions in conduction-band quantum wells *Phys. Rev. B* **50** 7474–82
- [79] Guillot F, Amstatt B, Bellet-Amalric E, Monroy E, Nevou L, Doyennette L, Julien F H and Dang L S 2006 Effect of Si doping on GaN/AlN multiple-quantum-well structures for intersubband optoelectronics at telecommunication wavelengths *Superlatt. Microstruct.* **40** 306–12
- [80] Berland K, Stattin M, Farivar R, Sultan D M S, Hyldgaard P, Larsson A, Wang S M and Andersson T G 2010 Temperature stability of intersubband transitions in AlN/GaN quantum wells *Appl. Phys. Lett.* **97** 043507
- [81] Liu X Y, Holmström P, Jänes P, Thylén L and Andersson T G 2007 Intersubband absorption at 1.5–3.5  $\mu\text{m}$  in GaN/AlN multiple quantum wells grown by molecular beam epitaxy on sapphire *Phys. Status Solidi B* **244** 2892–905
- [82] Suzuki N and Iizuka N 1999 Effect of polarization field on intersubband transition in AlGaIn/GaN quantum wells *Japan. J. Appl. Phys.* **38** L363–5
- [83] Ng H M, Gmachl C, Siegrist T, Chu S N G and Cho A Y 2001 Growth and characterization of GaN/AlGaIn superlattices for near-infrared intersubband transitions *Phys. Status Solidi a* **188** 825–31
- [84] Ng H M, Gmachl C, Heber J D, Hsu J W P, Chu S N G and Cho A Y 2002 Recent progress in GaN-based superlattices for near-infrared intersubband transitions *Phys. Status Solidi b* **234** 817–21
- [85] Sherliker B *et al* 2007 Room temperature operation of AlGaIn/GaN quantum well infrared photodetectors at a 3–4  $\mu\text{m}$  wavelength range *Semicond. Sci. Technol.* **22** 1240–4
- [86] Péré-Laperne N, Bayram C, Nguyen-The L, McClintock R and Razeghi M 2009 Tunability of intersubband absorption from 4.5 to 5.3  $\mu\text{m}$  in a GaN/Al<sub>0.2</sub>Ga<sub>0.8</sub>N superlattices grown by metalorganic chemical vapor deposition *Appl. Phys. Lett.* **95** 131109
- [87] Tian W *et al* 2012 Tunability of intersubband transition wavelength in the atmospheric window in AlGaIn/GaN multi-quantum wells grown on different AlGaIn templates by metalorganic chemical vapor deposition *J. Appl. Phys.* **112** 063526
- [88] Bayram C 2012 High-quality AlGaIn/GaN superlattices for near- and mid-infrared intersubband transitions *J. Appl. Phys.* **111** 013514
- [89] Huang C C *et al* 2011 Intersubband transitions at atmospheric window in Al<sub>x</sub>Ga<sub>1-x</sub>N/GaN multiple quantum wells grown on GaN/sapphire templates adopting AlN/GaN superlattices interlayer *Appl. Phys. Lett.* **98** 132105
- [90] Edmunds C, Tang L, Li D, Cervantes M, Gardner G, Paskova T, Manfra M J and Malis O 2012 Near-infrared absorption in lattice-matched AlInN/GaN and strained AlGaIn/GaN heterostructures grown by MBE on low-defect GaN substrates *J. Electron. Mater.* **41** 881–6
- [91] Machhadani H, Kotsar Y, Sakr S, Tchernycheva M, Colombelli R, Mangeney J, Bellet-Amalric E, Sarigiannidou E, Monroy E and Julien F H 2010 Terahertz intersubband absorption in GaN/AlGaIn step quantum wells *Appl. Phys. Lett.* **97** 191101
- [92] Edmunds C, Tang L, Shao J, Li D, Cervantes M, Gardner G, Zakharov D N, Manfra M J and Malis O 2012 Improvement of near-infrared absorption linewidth in AlGaIn/GaN superlattices by optimization of delta-doping location *Appl. Phys. Lett.* **101** 102104
- [93] Suzuki N, Iizuka N and Kaneko K 2003 Calculation of near-infrared intersubband absorption spectra in GaN/AlN quantum wells *Japan. J. Appl. Phys.* **42** 132–9
- [94] Tchernycheva M, Nevou L, Doyennette L, Julien F H, Guillot F, Monroy E, Remmele T and Albrecht M 2006 Electron confinement in strongly coupled GaN/AlN quantum wells *Appl. Phys. Lett.* **88** 153113
- [95] Driscoll K, Bhattacharyya A, Moustakas T D, Paiella R, Zhou L and Smith D J 2007 Intersubband absorption in AlN/GaN/AlGaIn coupled quantum wells *Appl. Phys. Lett.* **91** 141104
- [96] Cen L B, Shen B, Qin Z X and Zhang G Y 2009 Influence of polarization induced electric fields on the wavelength and the refractive index of intersubband transitions in AlN/GaN coupled double quantum wells *J. Appl. Phys.* **105** 093109
- [97] Cen L B, Shen B, Qin Z X and Zhang G Y 2009 Near-infrared two-color intersubband transitions in AlN/GaN coupled double quantum wells *J. Appl. Phys.* **105** 053106
- [98] Lupu A *et al* 2008 Lattice-matched GaN-InAlN waveguides at  $\lambda = 1.55 \mu\text{m}$  grown by metal-organic vapor phase epitaxy *IEEE Photon. Technol. Lett.* **20** 102–4
- [99] Nicolay S, Carlin J-F, Feltin E, Butté R, Mosca M, Grandjean N, Ilegems M, Tchernycheva M, Nevou L and Julien F H 2005 Midinfrared intersubband absorption in lattice-matched AlInN/GaN multiple quantum wells *Appl. Phys. Lett.* **87** 111106
- [100] Nicolay S, Feltin E, Carlin J-F, Mosca M, Nevou L, Tchernycheva M, Julien F H, Ilegems M and Grandjean N 2006 Indium surfactant effect on AlN/GaN heterostructures grown by metal-organic vapor-phase epitaxy: applications to intersubband transitions *Appl. Phys. Lett.* **88** 151902
- [101] Gonschorek M, Carlin J-F, Feltin E, Py M A, Grandjean N, Darakchieva V, Monemar B, Lorenz M and Ramm G 2008 Two-dimensional electron gas density in Al<sub>1-x</sub>In<sub>x</sub>N/AlN/GaN heterostructures ( $0.03 \leq x < 0.23$ ) *J. Appl. Phys.* **103** 093714
- [102] Malis O, Edmunds C, Manfra M J and Sivco D L 2009 Near-infrared intersubband absorption in molecular-beam epitaxy-grown lattice-matched InAlN/GaN superlattices *Appl. Phys. Lett.* **94** 161111
- [103] Cywiński G *et al* 2006 Growth of thin AlInN/GaInN quantum wells for applications to high-speed intersubband devices at telecommunication wavelengths *J. Vac. Sci. Technol. B* **24** 1505–9
- [104] Kudrawiec R, Motyka M, Cywin'ski G, Siekacz M, Skierbiszewski C, Nevou L, Doyennette L, Tchernycheva M, Julien F H and Misiewicz J 2008 Contactless electroluminescence spectroscopy of inter- and intersub-band transitions in AlInN/GaInN quantum wells *Phys. Status Solidi c* **5** 503–7
- [105] Akabli H, Almagoussi A, Abounadi A, Rajira A, Berland K and Andersson T G 2012 Intersubband energies in Al<sub>1-x</sub>In<sub>y</sub>N/Ga<sub>1-x</sub>In<sub>x</sub>N heterostructures with lattice constant close to a GaN *Superlatt. Microstruct.* **52** 70–77
- [106] Zhu J, Ban S-L and Ha S-H 2012 Phonon-assisted intersubband transitions in wurtzite GaN/In<sub>x</sub>Ga<sub>1-x</sub>N quantum wells *Chin. Phys. B* **21** 097301
- [107] Berryman K W, Lyon S A and Segev M 1997 Mid-infrared photoconductivity in InAs quantum dots *Appl. Phys. Lett.* **70** 1861–3
- [108] Phillips J, Kamath K and Bhattacharya P 1998 Far-infrared photoconductivity in self-organized InAs quantum dots *Appl. Phys. Lett.* **72** 2020–2
- [109] Ryzhii V 1996 The theory of quantum-dot infrared phototransistors *Semicond. Sci. Technol.* **11** 759–65
- [110] Pan D, Towe E and Kennerly S 1998 Normal-incidence intersubband (In, Ga)As/GaAs quantum dot infrared photodetectors *Appl. Phys. Lett.* **73** 1937–9
- [111] Chen Z, Baklenov O, Kim E T, Mukhametzhanov I, Tie J, Madhukar A, Ye Z and Campbell J C 2001 Normal incidence InAs/Al<sub>x</sub>Ga<sub>1-x</sub>As quantum dot infrared

- photodetectors with undoped active region *J. Appl. Phys.* **89** 4558–63
- [112] Chu L, Zrenner A, Bichler M and Abstreiter G 2001 Quantum-dot infrared photodetector with lateral carrier transport *Appl. Phys. Lett.* **79** 2249–51
- [113] Daudin B, Widmann F, Feuillet G, Samson Y, Arlery M and Rouvière J 1997 Stranski–Krastanov growth mode during the molecular beam epitaxy of highly strained GaN *Phys. Rev. B* **56** R7069–72
- [114] Chamard V, Schülly T, Sztucki M, Metzger T, Sarigiannidou E, Rouvière J-L, Tolan M and Adelman C 2004 Strain distribution in nitride quantum dot multilayers *Phys. Rev. B* **69** 125327
- [115] Sarigiannidou E, Monroy E, Daudin B, Rouvière J L and Andreev A D 2005 Strain distribution in GaN/AlN quantum-dot superlattices *Appl. Phys. Lett.* **87** 203112
- [116] Guillot F *et al* 2006 Si-doped GaN/AlN quantum dot superlattices for optoelectronics at telecommunication wavelengths *Phys. Status Solidi a* **203** 1754–8
- [117] Damilano B, Grandjean N, Sémoud F, Massies J and Leroux M 1999 From visible to white light emission by GaN quantum dots on Si(1 1 1) substrate *Appl. Phys. Lett.* **75** 962–4
- [118] Tanaka S, Iwai S and Aoyagi Y 1996 Self-assembling GaN quantum dots on  $\text{Al}_x\text{Ga}_{1-x}\text{N}$  surfaces using a surfactant *Appl. Phys. Lett.* **69** 4096–8
- [119] Ramvall P, Riblet P, Nomura S, Aoyagi Y and Tanaka S 2000 Optical properties of GaN quantum dots *J. Appl. Phys.* **87** 3883–90
- [120] Miyamura M, Tachibana K and Arakawa Y 2002 High-density and size-controlled GaN self-assembled quantum dots grown by metalorganic chemical vapor deposition *Appl. Phys. Lett.* **80** 3937–9
- [121] Andreev A and O'Reilly E 2000 Theory of the electronic structure of GaN/AlN hexagonal quantum dots *Phys. Rev. B* **62** 15851–70
- [122] Andreev A D and O'Reilly E P 2001 Optical transitions and radiative lifetime in GaN/AlN self-organized quantum dots *Appl. Phys. Lett.* **79** 521–3
- [123] Williams D, Andreev A, O'Reilly E and Faux D 2005 Derivation of built-in polarization potentials in nitride-based semiconductor quantum dots *Phys. Rev. B* **72** 235318
- [124] Ranjan V, Allan G, Priester C and Delerue C 2003 Self-consistent calculations of the optical properties of GaN quantum dots *Phys. Rev. B* **68** 115303
- [125] Moumanis K, Helman A, Fossard F, Tchernycheva M, Lusson A, Julien F H, Damilano B, Grandjean N and Massies J 2003 Intraband absorptions in GaN/AlN quantum dots in the wavelength range of 1.27–2.4  $\mu\text{m}$  *Appl. Phys. Lett.* **82** 868–70
- [126] Tchernycheva M, Nevou L, Doyennette L, Helman A, Colombelli R, Julien F H, Guillot F, Monroy E, Shibata T and Tanaka M 2005 Intraband absorption of doped GaN/AlN quantum dots at telecommunication wavelengths *Appl. Phys. Lett.* **87** 101912
- [127] Vardi A, Bahir G, Schacham S E, Kandaswamy P K and Monroy E 2009 Photocurrent spectroscopy of bound-to-bound intraband transitions in GaN/AlN quantum dots *Phys. Rev. B* **80** 155439
- [128] Nguyen D T, Wüster W, Roussignol P, Voisin C, Cassaboïs G, Tchernycheva M, Julien F H, Guillot F and Monroy E 2010 Homogeneous linewidth of the intraband transition at 1.55  $\mu\text{m}$  in GaN/AlN quantum dots *Appl. Phys. Lett.* **97** 061903
- [129] Himwas C, Songmuang R, Dang L S, Bleuse J, Rapenne L, Sarigiannidou E and Monroy E 2012 Thermal stability of the deep ultraviolet emission from AlGaIn/AlN Stranski–Krastanov quantum dots *Appl. Phys. Lett.* **101** 241914
- [130] Speck J S and Chichibu S F 2011 Nonpolar and semipolar group III nitride-based materials *MRS Bull.* **34** 304–12
- [131] Romanov A E, Baker T J, Nakamura S, Speck J S and ERATO/JST UCSB Group 2006 Strain-induced polarization in wurtzite III-nitride semipolar layers *J. Appl. Phys.* **100** 023522
- [132] Lahourcade L, Bellet-Amalric E, Monroy E, Abouzaid M and Ruterana P 2007 Plasma-assisted molecular-beam epitaxy of AlN(11–22) on m sapphire *Appl. Phys. Lett.* **90** 131909
- [133] Lahourcade L, Kandaswamy P K, Renard J, Ruterana P, Machhadani H, Tchernycheva M, Julien F H, Gayral B and Monroy E 2008 Interband and intersubband optical characterization of semipolar (1122)-oriented GaN/AlN multiple-quantum-well structures *Appl. Phys. Lett.* **93** 111906
- [134] Gmachl C and Ng H M 2003 Intersubband absorption at  $\sim 2.1 \mu\text{m}$  in A-plane GaN/AlN multiple quantum wells *Electron. Lett.* **39** 567–9
- [135] Brazis R and Raguotis R 2006 Monte Carlo modeling of phonon-assisted carrier transport in cubic and hexagonal gallium nitride *Opt. Quantum Electron.* **38** 339–47
- [136] Pugh S K, Dugdale D J, Brand S and Abram R A 1999 Electronic structure calculations on nitride semiconductors *Semicond. Sci. Technol.* **14** 23–31
- [137] Suzuki M and Uenoyama T 1996 Optical gain and crystal symmetry in III–V nitride lasers *Appl. Phys. Lett.* **69** 3378–80
- [138] DeCuir E A, Fred E, Manasreh M O, Schörmann J, As D J and Lischka K 2007 Near-infrared intersubband absorption in nonpolar cubic GaN/AlN superlattices *Appl. Phys. Lett.* **91** 041911
- [139] Machhadani H, Tchernycheva M, Sakr S, Rigutti L, Colombelli R, Warde E, Mietze C, As D J and Julien F H 2011 Intersubband absorption of cubic GaN/Al(Ga)N quantum wells in the near-infrared to terahertz spectral range *Phys. Rev. B* **83** 075313
- [140] Noda S, Yamashita T, Ohya M, Muromoto Y and Sasaki A 1993 All-optical modulation for semiconductor lasers by using three energy levels in n-doped quantum wells *IEEE J. Quantum Electron.* **29** 1640–7
- [141] Wada O 2004 Femtosecond all-optical devices for ultrafast communication and signal processing *New J. Phys.* **6** 183
- [142] Iizuka N, Kaneko K, Suzuki N, Asano T, Noda S and Wada O 2000 Ultrafast intersubband relaxation ( $\leq 150$  fs) in AlGaIn/GaN multiple quantum wells *Appl. Phys. Lett.* **77** 648–50
- [143] Gmachl C, Frolov S V, Ng H M, Chu S-N G and Cho A Y 2001 Sub-picosecond electron scattering time for  $\lambda = 1.55 \mu\text{m}$  intersubband transitions in GaN/AlGaIn multiple quantum wells *Electron. Lett.* **37** 378
- [144] Rapaport R, Chen G, Mitrofanov O, Gmachl C, Ng H M and Chu S N G 2003 Resonant optical nonlinearities from intersubband transitions in GaN/AlN quantum wells *Appl. Phys. Lett.* **83** 263
- [145] Iizuka N, Kaneko K and Suzuki N 2005 Sub-picosecond all-optical gate utilizing GaN intersubband transition *Opt. Express* **13** 3835–40
- [146] Hamazaki J, Kunugita H, Ema K, Kikuchi A and Kishino K 2005 Intersubband relaxation dynamics in GaN/AlN multiple quantum wells studied by two-color pump-probe experiments *Phys. Rev. B* **71** 165334
- [147] Suzuki N, Iizuka N and Kaneko K 2000 Intersubband transition in AlGaIn–GaN quantum wells for ultrafast all-optical switching at communication wavelength *Proc. SPIE* **3940** 127–38



- [148] Iizuka N, Kaneko K and Suzuki N 2004 Sub-picosecond modulation by intersubband transition in ridge waveguide with GaN/AlN quantum wells *Electron. Lett.* **40** 962963
- [149] Li Y, Bhattacharyya A, Thomidis C, Moustakas T D and Paiella R 2007 Ultrafast all-optical switching with low saturation energy via intersubband transitions in GaN/AlN quantum-well waveguides *Opt. Express* **15** 17922–7
- [150] Sodabanlu H, Yang J-S, Tanemura T, Sugiyama M, Shimogaki Y and Nakano Y 2011 Intersubband absorption saturation in AlN-based waveguide with GaN/AlN multiple quantum wells grown by metalorganic vapor phase epitaxy *Appl. Phys. Lett.* **99** 151102
- [151] Iizuka N, Yoshida H, Managaki N, Shimizu T, Hassanet S, Cumtornkittikul C, Sugiyama M and Nakano Y 2009 Integration of GaN/AlN all-optical switch with SiN/AlN waveguide utilizing spot-size conversion *Opt. Express* **17** 23247–53
- [152] Iizuka N, Kaneko K and Suzuki N 2006 Polarization dependent loss in III-nitride optical waveguides for telecommunication devices *J. Appl. Phys.* **99** 093107
- [153] Sun G, Khurgin J B and Soref R A 2005 Nonlinear all-optical GaN/AlGaIn multi-quantum-well devices for 100 Gb/s applications at  $\lambda = 1.55 \mu\text{m}$  *Appl. Phys. Lett.* **87** 201108
- [154] Li Y and Paiella R 2006 Intersubband all-optical switching based on Coulomb-induced optical nonlinearities in GaN/AlGaIn coupled quantum wells *Semicond. Sci. Technol.* **21** 1105–10
- [155] Valdueza-Felip S, Naranjo F B, Gonzalez-Herraez M, Fernandez H, Solis J, Guillot F, Monroy E, Nevou L, Tchernycheva M and Julien F H 2008 Characterization of the resonant third-order nonlinear susceptibility of Si-Doped GaN–AlN quantum wells and quantum dots at  $1.5 \mu\text{m}$  *IEEE Photon. Technol. Lett.* **20** 1366–8
- [156] Suzuki S, Asada M, Teranishi A, Sugiyama H and Yokoyama H 2010 Fundamental oscillation of resonant tunneling diodes above 1 THz at room temperature *Appl. Phys. Lett.* **97** 242102
- [157] Feiginov M, Sydlo C, Cojocari O and Meissner P 2011 Resonant-tunnelling-diode oscillators operating at frequencies above 1.1 THz *Appl. Phys. Lett.* **99** 233506
- [158] Leconte S, Guillot F, Sarigiannidou E and Monroy E 2007 Charge distribution and vertical electron transport through GaN/AlN/GaN single-barrier structures *Semicond. Sci. Technol.* **22** 107–12
- [159] Leconte S, Gerrer L and Monroy E 2009 Electronic transport through GaN/AlN single barriers: effect of polarisation and dislocations *Microelectron. J.* **40** 339–41
- [160] Simpkins B S, Yu E T, Waltereit P and Speck J S 2003 Correlated scanning kelvin probe and conductive atomic force microscopy studies of dislocations in gallium nitride *J. Appl. Phys.* **94** 1448–53
- [161] Simon J, Zhang Z, Goodman K, Xing H, Kosel T, Fay P and Jena D 2009 Polarization-induced zener tunnel junctions in wide-band-gap heterostructures *Phys. Rev. Lett.* **103** 026801
- [162] Grinyaev S N and Razzhuvalov A N 2001 Resonant electron tunneling in GaN/Ga<sub>1-x</sub>Al<sub>x</sub>N(0001) strained structures with spontaneous polarization and piezoeffect *Phys. Solid State* **43** 549–55
- [163] Kikuchi A, Bannai R, Kishino K, Lee C-M and Chyi J-I 2002 AlN/GaN double-barrier resonant tunneling diodes grown by rf-plasma-assisted molecular-beam epitaxy *Appl. Phys. Lett.* **81** 1729–31
- [164] Foxon C T *et al* 2003 Current–voltage instabilities in GaN/AlGaIn resonant tunnelling structures *Phys. Status Solidi c* **0** 2389–92
- [165] Belyaev A E, Foxon C T, Novikov S V, Makarovskiy O, Eaves L, Kappers M J and Humphreys C J 2003 Comment on ‘AlN/GaN double-barrier resonant tunneling diodes grown by rf-plasma-assisted molecular-beam epitaxy’ *Appl. Phys. Lett.* **83** 3626
- [166] Kikuchi A, Bannai R, Kishino K, Lee C-M and Chyi J-I 2003 Response to ‘Comment on “AlN/GaN double-barrier resonant tunneling diodes grown by rf-plasma-assisted molecular-beam epitaxy”’ *Appl. Phys. Lett.* **83** 3628
- [167] Indlekofer K M, Donà E, Malindretos J, Bertelli M, Kocan M, Rizzi A and Lüth H 2002 Modelling of polarization charge-induced asymmetry of I–V characteristics of AlN/GaN-based resonant tunnelling structures *Phys. Status Solidi b* **234** 769–72
- [168] Sacconi F, Di Carlo A and Lugli P 2002 Modeling of GaN-based resonant tunneling diodes: influence of polarization fields *Phys. Status Solidi a* **190** 295–9
- [169] Sakr S, Warde E, Tchernycheva M and Julien F H 2011 Ballistic transport in GaN/AlGaIn resonant tunneling diodes *J. Appl. Phys.* **109** 023717
- [170] Berland K, Andersson T and Hyldgaard P 2011 Polarization-balanced design of heterostructures: application to AlN/GaN double-barrier structures *Phys. Rev. B* **84** 245313
- [171] Warde E, Sakr S, Tchernycheva M and Julien F H 2012 Vertical transport in GaN/AlGaIn resonant tunneling diodes and superlattices *J. Electron. Mater.* **41** 965–70
- [172] Hermann M, Monroy E, Helman A, Baur B, Albrecht M, Daudin B, Ambacher O, Stutzmann M and Eickhoff M 2004 Vertical transport in group III-nitride heterostructures and application in AlN/GaN resonant tunneling diodes *Phys. Status Solidi c* **1** 2210–27
- [173] Golka S, Pflügl C, Schrenk W, Strasser G, Skierbiszewski C, Siekacz M, Grzegory I and Porowski S 2006 Negative differential resistance in dislocation-free GaN/AlGaIn double-barrier diodes grown on bulk GaN *Appl. Phys. Lett.* **88** 172106
- [174] Kurakin A M, Vitusevich S A, Danylyuk S V, Naumov A V, Foxon C T, Novikov S V, Klein N, Lüth H and Belyaev A E 2006 Capacitance characterization of AlN/GaN double-barrier resonant tunnelling diodes *Phys. Status Solidi c* **3** 2265–9
- [175] Vashaei Z, Bayram C and Razeghi M 2010 Demonstration of negative differential resistance in GaN/AlN resonant tunneling diodes at room temperature *J. Appl. Phys.* **107** 083505
- [176] Bayram C, Vashaei Z and Razeghi M 2010 Room temperature negative differential resistance characteristics of polar III-nitride resonant tunneling diodes *Appl. Phys. Lett.* **97** 092104
- [177] Bayram C, Vashaei Z and Razeghi M 2010 AlN/GaN double-barrier resonant tunneling diodes grown by metal-organic chemical vapor deposition *Appl. Phys. Lett.* **96** 042103
- [178] Bayram C, Vashaei Z and Razeghi M 2010 Reliability in room-temperature negative differential resistance characteristics of low-aluminum content AlGaIn/GaN double-barrier resonant tunneling diodes *Appl. Phys. Lett.* **97** 181109
- [179] Petrychuk M V, Belyaev A E, Kurakin A M, Danylyuk S V, Klein N and Vitusevich S A 2007 Mechanisms of current formation in resonant tunneling AlN/GaN heterostructures *Appl. Phys. Lett.* **91** 222112
- [180] Boucherit M, Soltani A, Monroy E, Rousseau M, Deresmes D, Berthe M, Durand C and De Jaeger J-C 2011 Investigation of the negative differential resistance reproducibility in AlN/GaN double-barrier resonant tunnelling diodes *Appl. Phys. Lett.* **99** 182109
- [181] Sakr S, Kotsar Y, Tchernycheva M, Warde E, Isac N, Monroy E and Julien F H 2012 Resonant tunneling transport in a GaN/AlN multiple-quantum-well structure *Appl. Phys. Express* **5** 052203



- [182] Björk M T, Ohlsson B J, Thelander C, Persson A I, Deppert K, Wallenberg L R and Samuelson L 2002 Nanowire resonant tunneling diodes *Appl. Phys. Lett.* **81** 4458–60
- [183] Songmuang R, Katsaros G, Monroy E, Spathis P, Bougerol C, Mongillo M and De Franceschi S 2010 Quantum transport in GaN/AlN double-barrier heterostructure nanowires *Nano Lett.* **10** 3545–50
- [184] Rigutti L, Jacopin G, Bugallo A D L, Tchernycheva M, Warde E, Julien F H, Songmuang R, Galopin E, Largeau L and Harmand J-C 2010 Investigation of the electronic transport in GaN nanowires containing GaN/AlN quantum discs *Nanotechnology* **21** 425206
- [185] Carnevale S D, Marginean C, Phillips P J, Kent T F, Sarwar A T M G, Mills M J and Myers R C 2012 Coaxial nanowire resonant tunneling diodes from non-polar AlN/GaN on silicon *Appl. Phys. Lett.* **100** 142115
- [186] Lewen R, Irmscher S, Westergren U, Thylen L and Eriksson U 2004 Segmented transmission-line electroabsorption modulators *J. Lightwave Technol.* **22** 172–9
- [187] Kondo J *et al* 2005 High-speed and low-driving-voltage thin-sheet X-cut LiNbO<sub>3</sub> modulator with laminated low-dielectric-constant adhesive *IEEE Photon. Technol. Lett.* **17** 2077–9
- [188] Holmstrom P 2001 High-speed mid-IR modulator using stark shift in step quantum wells *IEEE J. Quantum Electron.* **37** 1273–82
- [189] Holmstrom P 2006 Electroabsorption modulator using intersubband transitions in GaN–AlGaIn–AlN step quantum wells *IEEE J. Quantum Electron.* **42** 810–9
- [190] Holmström P, Liu X Y, Uchida H, Aggerstam T, Kikuchi A, Kishino K, Lourduos S, Andersson T G and Thylén L 2007 Intersubband photonic devices by group-III nitrides *Proc. SPIE* **6782** 67821N
- [191] Baumann E, Giorgetta F R, Hofstetter D, Leconte S, Guillot F, Bellet-Amalric E and Monroy E 2006 Electrically adjustable intersubband absorption of a GaN/AlN superlattice grown on a transistorlike structure *Appl. Phys. Lett.* **89** 101121
- [192] Nevou L *et al* 2007 Short-wavelength intersubband electroabsorption modulation based on electron tunneling between GaN/AlN coupled quantum wells *Appl. Phys. Lett.* **90** 223511
- [193] Kheirodin N *et al* 2008 Electrooptical modulator at telecommunication wavelengths based on GaN/AlN coupled quantum wells *IEEE Photon. Technol. Lett.* **20** 724–6
- [194] Dussaigne A *et al* 2010 Growth of intersubband GaN/AlGaIn heterostructures *Proc. SPIE* **7608** 76080H
- [195] Dupont E B, Delacourt D and Papuchon M 1993 Mid-infrared phase modulation via Stark effect on intersubband transitions in GaAs/GaAlAs quantum wells *IEEE J. Quantum Electron.* **29** 2313–8
- [196] Li Y, Bhattacharyya A, Thomidis C, Liao Y, Moustakas T D and Paiella R 2008 Refractive-index nonlinearities of intersubband transitions in GaN/AlN quantum-well waveguides *J. Appl. Phys.* **104** 083101
- [197] Lupu A, Tchernycheva M, Kotsar Y, Monroy E and Julien F H 2012 Electroabsorption and refractive index modulation induced by intersubband transitions in GaN/AlN multiple quantum wells *Opt. Express* **20** 12541
- [198] Gross E, Pesach A, Monroy E, Schacham S E and Bahir G 2013 Direct measurement of refractive index change around intersubband transition resonance using free-space Mach–Zehnder interferometer *Opt. Express* **21** 3800–8
- [199] Zucker J E, Bar-Joseph I, Miller B I, Koren U and Chemla D S 1989 Quaternary quantum wells for electro-optic intensity and phase modulation at 1.3 and 1.55  $\mu\text{m}$  *Appl. Phys. Lett.* **54** 10–2
- [200] Soref R and Bennett B 1987 Electrooptical effects in silicon *IEEE J. Quantum Electron.* **23** 123–9
- [201] Hofstetter D, Schad S-S, Wu H, Schaff W J and Eastman L F 2003 GaN/AlN-based quantum-well infrared photodetector for 1.55  $\mu\text{m}$  *Appl. Phys. Lett.* **83** 572–4
- [202] Baumann E, Giorgetta F R, Hofstetter D, Lu H, Chen X, Schaff W J, Eastman L F, Golka S, Schrenk W and Strasser G 2005 Intersubband photoconductivity at 1.6  $\mu\text{m}$  using strain-compensated AlN/GaN superlattice *Appl. Phys. Lett.* **87** 191102
- [203] DeCuir E A, Manasreh M O, Tschumak E, Schörmann J, As D J and Lischka K 2008 Cubic GaN/AlN multiple quantum well photodetector *Appl. Phys. Lett.* **92** 201910
- [204] Doyennette L, Nevou L, Tchernycheva M, Lupu A, Guillot F, Monroy E, Colombelli R and Julien F H 2005 GaN-based quantum dot infrared photodetector operating at 1.38  $\mu\text{m}$  *Electron. Lett.* **41** 1077–8
- [205] Vardi A, Akopian N, Bahir G, Doyennette L, Tchernycheva M, Nevou L, Julien F H, Guillot F and Monroy E 2006 Room temperature demonstration of GaN/AlN quantum dot intraband infrared photodetector at fiber-optics communication wavelength *Appl. Phys. Lett.* **88** 143101
- [206] Vardi A, Bahir G, Schacham S E, Kandaswamy P K and Monroy E 2010 Negative photoconductivity due to intraband transitions in GaN/AlN quantum dots *J. Appl. Phys.* **108** 104512
- [207] Baumann E, Giorgetta F R, Hofstetter D, Wu H, Schaff W J, Eastman L F and Kirste L 2005 Tunneling effects and intersubband absorption in AlN/GaN superlattices *Appl. Phys. Lett.* **86** 032110
- [208] Reshchikov M A and Morkoç H 2005 Luminescence properties of defects in GaN *J. Appl. Phys.* **97** 061301
- [209] Monroy E, Omn s F and Calle F 2003 Wide-bandgap semiconductor ultraviolet photodetectors *Semicond. Sci. Technol.* **18** R33–51
- [210] Hofstetter D, Baumann E, Giorgetta F R, Graf M, Maier M, Guillot F, Bellet-Amalric E and Monroy E 2006 High-quality AlN/GaN-superlattice structures for the fabrication of narrow-band 1.4  $\mu\text{m}$  photovoltaic intersubband detectors *Appl. Phys. Lett.* **88** 121112
- [211] Giorgetta F R, Baumann E, Guillot F, Monroy E and Hofstetter D 2007 High frequency ( $f = 2.37$  GHz) room temperature operation of 1.55  $\mu\text{m}$  AlN/GaN-based intersubband detector *Electron. Lett.* **43** 185–7
- [212] Hofstetter D *et al* 2009 Photodetectors based on intersubband transitions using III-nitride superlattice structures *J. Phys.: Condens. Matter* **21** 174208
- [213] Rosencher E and Bois P 1991 Model system for optical nonlinearities: asymmetric quantum wells *Phys. Rev. B* **44** 11315–27
- [214] Hofstetter D, Di Francesco J, Kandaswamy P K, Das A, Valdeuza-Felip S and Monroy E 2010 Performance improvement of AlN/GaN-based intersubband detectors by using quantum dots *IEEE Photon. Technol. Lett.* **22** 1087–9
- [215] Hofstetter D, Theron R, Baumann E, Giorgetta F R, Golka S, Strasser G, Guillot F and Monroy E 2008 Monolithically integrated AlGaIn/GaN/AlN-based solar-blind ultraviolet and near-infrared detectors *Electron. Lett.* **44** 986
- [216] Hofstetter D, Baumann E, Giorgetta F R, Theron R, Guillot F, Monroy E, Golka S and Strasser G 2009 Monolithically integrated UV/IR-photodetectors based on an AlN/GaN-based superlattice grown on an AlGaIn buffer layer *Phys. Status Solidi c* **6** S818–21

- [217] Gendron L, Carras M, Huynh A, Ortiz V, Koeniguer C and Berger V 2004 Quantum cascade photodetector *Appl. Phys. Lett.* **85** 2824
- [218] Giorgetta F R *et al* 2009 Quantum cascade detectors *IEEE J. Quantum Electron.* **45** 1039–52
- [219] Vardi A, Bahir G, Guillot F, Bougerol C, Monroy E, Schacham S E, Tchernycheva M and Julien F H 2008 Near infrared quantum cascade detector in GaN/AlGaIn/AlN heterostructures *Appl. Phys. Lett.* **92** 011112
- [220] Sakr S, Kotsar Y, Haddadi S, Tchernycheva M, Vivien L, Sarigiannidou I, Isac N, Monroy E and Julien F H 2010 GaN-based quantum cascade photodetector with 1.5  $\mu\text{m}$  peak detection wavelength *Electron. Lett.* **46** 1685–6
- [221] Vardi A *et al* 2008 High-speed operation of GaN/AlGaIn quantum cascade detectors at  $\lambda \approx 1.55 \mu\text{m}$  *Appl. Phys. Lett.* **93** 193509
- [222] Vardi A, Sakr S, Mangeney J, Kandaswamy P K, Monroy E, Tchernycheva M, Schacham S E, Julien F H and Bahir G 2011 Femto-second electron transit time characterization in GaN/AlGaIn quantum cascade detector at 1.5  $\mu\text{m}$  *Appl. Phys. Lett.* **99** 202111
- [223] Gryshchenko S V, Klymenko M V, Shulika O V, Sukhoivanov I A and Lysak V V 2012 Temperature dependence of electron transport in GaN/AlGaIn quantum cascade detectors *Superlatt. Microstruct.* **52** 894–900
- [224] Sakr S *et al* 2013 GaN/AlGaIn waveguide quantum cascade photodetectors at  $\lambda \approx 1.55 \mu\text{m}$  with enhanced responsivity and  $\sim 40$  GHz frequency bandwidth *Appl. Phys. Lett.* **102** 011135
- [225] Sakr S, Giraud E, Dussaigne A, Tchernycheva M, Grandjean N and Julien F H 2012 Two-color GaN/AlGaIn quantum cascade detector at short infrared wavelengths of 1 and 1.7  $\mu\text{m}$  *Appl. Phys. Lett.* **100** 181103
- [226] Sakr S, Giraud E, Tchernycheva M, Isac N, Quach P, Warde E, Grandjean N and Julien F H 2012 A simplified GaN/AlGaIn quantum cascade detector with an alloy extractor *Appl. Phys. Lett.* **101** 251101
- [227] Sudradjat F F, Zhang W, Woodward J, Durmaz H, Moustakas T D and Paiella R 2012 Far-infrared intersubband photodetectors based on double-step III-nitride quantum wells *Appl. Phys. Lett.* **100** 241113
- [228] Nevou L, Julien F H, Colombelli R, Guillot F and Monroy E 2006 Room-temperature intersubband emission of GaN/AlN quantum wells at  $\lambda = 2.3 \mu\text{m}$  *Electron. Lett.* **42** 1308–9
- [229] Nevou L, Tchernycheva M, Julien F H, Guillot F and Monroy E 2007 Short wavelength ( $\lambda = 2.13 \mu\text{m}$ ) intersubband luminescence from GaN/AlN quantum wells at room temperature *Appl. Phys. Lett.* **90** 121106
- [230] Driscoll K, Liao Y, Bhattacharyya A, Zhou L, Smith D J, Moustakas T D and Paiella R 2009 Optically pumped intersubband emission of short-wave infrared radiation with GaN/AlN quantum wells *Appl. Phys. Lett.* **94** 081120
- [231] Nevou L, Julien F H, Tchernycheva M, Guillot F, Monroy E and Sarigiannidou E 2008 Intraband emission at  $\lambda \approx 1.48 \mu\text{m}$  from GaN/AlN quantum dots at room temperature *Appl. Phys. Lett.* **92** 161105
- [232] Jovanović V D, Ikonić Z, Indjin D, Harrison P, Milanović V and Soref R A 2003 Designing strain-balanced GaN/AlGaIn quantum well structures: application to intersubband devices at 1.3 and 1.55  $\mu\text{m}$  wavelengths *J. Appl. Phys.* **93** 3194–7
- [233] Stattin M, Berland K, Hyldgaard P, Larsson A and Andersson T G 2011 Waveguides for nitride based quantum cascade lasers *Phys. Status Solidi c* **8** 2357–9
- [234] Ive T, Berland K, Stattin M, Fälth F, Hyldgaard P, Larsson A and Andersson T G 2012 Design and fabrication of AlN/GaN heterostructures for intersubband technology *Japan. J. Appl. Phys.* **51** 01AG07
- [235] Köhler R, Tredicucci A, Beltram F, Beere H E, Linfield E H, Davies A G, Ritchie D A., Iotti R C and Rossi F 2002 Terahertz semiconductor-heterostructure laser *Nature* **417** 156–9
- [236] Scalari G, Walther C, Fischer M, Terazzi R, Beere H, Ritchie D and Faist J 2009 THz and sub-THz quantum cascade lasers *Laser Photon. Rev.* **3** 45–66
- [237] Williams B S 2007 Terahertz quantum-cascade lasers *Nature Photon.* **1** 517–25
- [238] Kumar S, Hu Q and Reno J L 2009 186 K operation of terahertz quantum-cascade lasers based on a diagonal design *Appl. Phys. Lett.* **94** 131105
- [239] Williams B S, Callebaut H, Hu Q and Reno J L 2001 Magnetotunneling spectroscopy of resonant anticrossing in terahertz intersubband emitters *Appl. Phys. Lett.* **79** 4444
- [240] Williams B S, Callebaut H, Kumar S, Hu Q and Reno J L 2003 3.4-THz quantum cascade laser based on longitudinal-optical-phonon scattering for depopulation *Appl. Phys. Lett.* **82** 1015–7
- [241] Lü J T and Cao J C 2006 Monte Carlo simulation of hot phonon effects in resonant-phonon-assisted terahertz quantum-cascade lasers *Appl. Phys. Lett.* **88** 061119
- [242] Jovanović V D, Indjin D, Ikonić Z and Harrison P 2004 Simulation and design of GaN/AlGaIn far-infrared ( $\lambda \sim 34 \mu\text{m}$ ) quantum-cascade laser *Appl. Phys. Lett.* **84** 2995–7
- [243] Sun G, Soref R A and Khurgin J B 2005 Active region design of a terahertz GaN/Al<sub>0.15</sub>Ga<sub>0.85</sub>N quantum cascade laser *Superlatt. Microstruct.* **37** 107–13
- [244] Vukmirović N, Jovanović V D, Indjin D, Ikonić Z, Harrison P and Milanović V 2005 Optically pumped terahertz laser based on intersubband transitions in a GaN/AlGaIn double quantum well *J. Appl. Phys.* **97** 103106
- [245] Bellotti E, Driscoll K, Moustakas T D and Paiella R 2008 Monte Carlo study of GaN versus GaAs terahertz quantum cascade structures *Appl. Phys. Lett.* **92** 101112
- [246] Terashima W and Hirayama H 2009 Design and fabrication of terahertz quantum cascade laser structure based on III-nitride semiconductors *Phys. Status Solidi c* **6** S615–8
- [247] Yasuda H, Kubis T and Hirakawa K 2011 Non-equilibrium Green's function calculation for GaN-based terahertz quantum cascade laser structures *IRMMW-THz: 36th Int. Conf. on Infrared, Millimeter and Terahertz Waves* 1–2
- [248] Chou H, Manzur T and Anwar M 2011 Active layer design of THz GaN quantum cascade lasers *Proc. SPIE* **8023** 802309
- [249] Mirzaei B, Rostami A and Baghban H 2012 Terahertz dual-wavelength quantum cascade laser based on GaN active region *Opt. Laser Technol.* **44** 378–83
- [250] Harrison P, Indjin D, Jovanović V D, Mirčetić A, Ikonić Z, Kelsall R W, McTavish J, Savić I, Vukmirović N and Milanović V 2005 A physical model of quantum cascade lasers: application to GaAs, GaN and SiGe devices *Phys. Status Solidi a* **202** 980–6
- [251] Terashima W and Hirayama H 2011 Spontaneous emission from GaN/AlGaIn terahertz quantum cascade laser grown on GaN substrate *Phys. Status Solidi c* **8** 2302–4
- [252] Terashima W and Hirayama H 2011 Terahertz intersubband electroluminescence from GaN/AlGaIn quantum cascade laser structure on AlGaIn template *IRMMW-THz: 36th Int. Conf. on Infrared, Millimeter and Terahertz Waves* 1–2
- [253] Bellotti E, Driscoll K, Moustakas T D and Paiella R 2009 Monte Carlo simulation of terahertz quantum cascade

- laser structures based on wide-bandgap semiconductors *J. Appl. Phys.* **105** 113103
- [254] Sudradjat F, Zhang W, Driscoll K, Liao Y, Bhattacharyya A, Thomidis C, Zhou L, Smith D J, Moustakas T D and Paiella R 2010 Sequential tunneling transport characteristics of GaN/AlGaIn coupled-quantum-well structures *J. Appl. Phys.* **108** 103704
- [255] Chou H, Anwar M and Manzur T 2012 Active layer design and power calculation of nitride-based THz quantum cascade lasers *Proc. SPIE* **8268** 82680O
- [256] Yasuda H, Hosako I and Hirakawa K 2012 Designs of GaN-based terahertz quantum cascade lasers for higher temperature operations *CLEO: Conf. on Lasers and Electro-Optics* 1–2